UNIVERSITÀ
DEGLI STUDI
FIRENZE

DOTTORATO DI RICERCA IN SCIENZE BIOMEDICHE

CICLO XXXIII

COORDINATORE Prof. Massimo Stefani

The structural dynamics of titin in situ and its role in contraction and relaxation of the striated muscle

Settore Scientifico Disciplinare BIO/09

Dottorando
Dott. Squarci Caterina

Caterina Squarci

Tutore
Prof. Piazzesi Gabriella

Gabriella Piazzesi

Prof. Pasquale Bianco

Pasquale Bianco

Coordinatore
Prof. Stefani Massimo

____
(firma)

Anni 2017/2021

E ricordati sempre,
timone al centro e avanti così..

A Nonno Luigi

Acknowledgments

Il lavoro di tesi segna la fine di un percorso che oltre ad essere la somma di ore di studio, di apprendimento, di esperimenti e di analisi, è anche la somma di tante anime.

Tra queste righe ci sono la determinazione di Vincenzo Lombardi con il quale ho condotto gli esperimenti e imparato a stare davanti ad un set up sperimentale. La pazienza di Gabriella Piazzesi che dopo avermi insegnato i segreti della dissezione mi ha scortato nel tortuoso mondo dell'analisi dei dati oltre ad avermi supportato durante la stesura di tutti miei elaborati. Ci sono i consigli ed i turni di notte al sincrotrone di Marco Linari e Massimo Reconditi, c'è la spensieratezza di Pasquale Bianco ed i mille talenti di Marco Caremani.

Oltre alle molte questioni scientifiche dietro queste pagine non manca una bella dose di "chiacchere da salotto" con Giulio che ha iniziato il dottorato insieme a me, Matteo e Ilaria che lo stanno portando avanti ma soprattutto con Irene, inestimabile compagna e punto di riferimento.

Grazie per tutto quello che avete fatto durante questo percorso, quasi mai facile, ma di sicuro stimolante.

Un enorme ringraziamento va poi ai miei genitori, Alessandro e Antonella, che mi hanno sempre spronato a seguire le mie passioni e supportato in ogni momento di crisi. A mia sorella Costanza che mi è sempre stata vicina e dato forza con il suo considerarmi "la sorella intelligente". A tutti i miei amici, in particolare alle mie adorabili F.Ninja, ma soprattutto al mio compagno Lorenzo che mi supporta e sopporta con (e nonostante) il dottorato di ricerca.

Index

Chapter 1. Introduction ***page 6***

1.1. Background *page 6*

  1.1.1. The sarcomere *page 7*

  1.1.2. The contractile proteins and the myofilaments *page 8*

1.2. Regulation of contraction *page 11*

1.3. The cytoskeleton protein titin *page 13*

1.4. The role of titin in the passive and active sarcomere *page 14*

1.5. Aims *page 16*

1.6. Summary of results *page 17*

Chapter 2. Methods ***page 19***

2.1 Preparation and mounting of the fibre *page 19*

  2.1.1 Muscle fibre preparation *page 19*

  2.1.2 Mounting of the fibre for mechanical experiments *page 19*

2.2 Fibre measurements *page 20*

2.3 Fibre stimulation *page 21*

2.4 Solutions *page 21*

2.5 Mechanical Setup *page 21*

  2.5.1 Force transducer *page 21*

  2.5.2 Loudspeaker motor *page 22*

  2.5.3 Striation follower *page 23*

2.6 Mechanical Protocol *page 25*

2.7 Mechanical data collection and analysis *page 27*

2.8 X-ray diffraction setup *page 28*

  2.8.1 Beamline characteristics *page 29*

  2.8.2 The FReLoN CCD-based detector *page 30*

  2.8.3 Signal generation and acquisition *page 30*

2.9 X-ray diffraction acquisition protocol *page 30*

2.10 X-ray diffraction data analysis *page 31*

Chapter 3. Results ***page 35***

3.1 PNB suppresses thick filament activation and motor attachment during tetanic stimulation and imposed stretch *page 35*

3.2 During tetanic stimulation the I-band titin extensibility reduces by one order of magnitude and becomes independent of SL *page 41*

3.3 Temperature does not affect the OFF and ON states of titin but controls the transition kinetics measured with 4kHz oscillations *page 45*

3.4 The OFF-ON transition is explained by binding of a titin domain distal to the proximal poly-Ig domain to the nearest actin monomer *page 52*

3.5 The kinetics of OFF-ON transition of the I-band titin is accounted for by Ca^{2+}-dependent thin filament activation *page 55*

Chapter 4. Discussion ***page 62***

4.1 How the dual state of titin bites into muscle contraction-relaxation *page 62*

4.2 Relation with existing *in situ* and *in vitro* studies on titin mechanics *page 64*

Chapter 5. Conclusions ***page 69***

References ***page 70***

Chapter 1. Introduction

1.1 Background

In each sarcomere, the ~2 µm long structural unit of striated muscle cell, force and shortening are generated by the cyclical interactions of the motor protein myosin II, arranged in two bipolar arrays on the thick filaments, with the nearby thin, actin-containing filaments originating at the sarcomere extremities (Fig. 1.1, see section 1.1).

An ATP-driven working stroke in the myosin head domain bound to actin generates the force that pulls the actin filament towards the centre of the sarcomere (Huxley, 1969; Huxley & Simmons, 1971; Lymn & Taylor, 1971; Rayment *et al.*, 1993a). The maximum force developed in an isometric tetanus (T_0) depends on the number of motors in the half-sarcomere, in which the myosin motors are mechanically coupled as parallel force generators available for actin-attachment, and thus on the degree of overlap between thick and thin filaments (Gordon *et al.*, 1966).

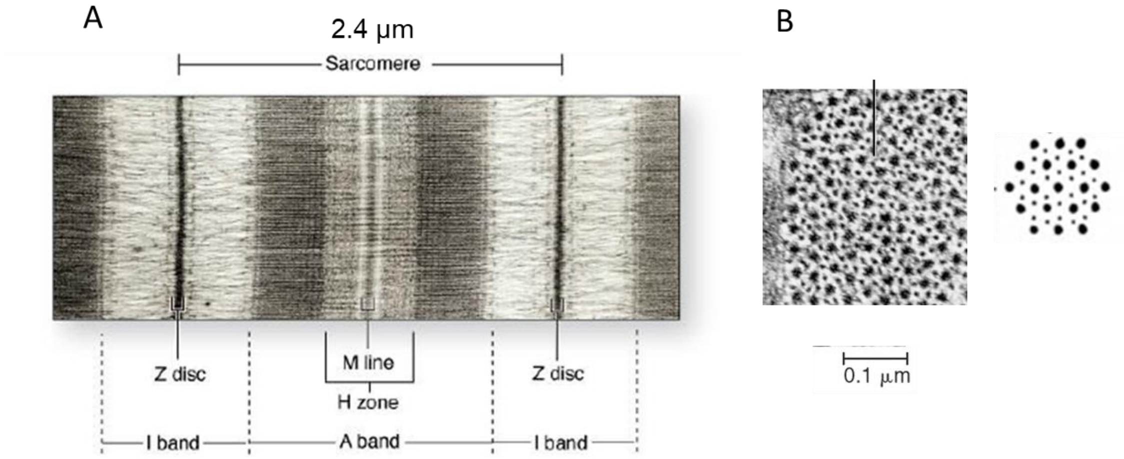

Figure 1.1. Electron micrograph of a sarcomere. A. Longitudinal section. **B.** Cross section.

In frog muscle T_0 is maximum at sarcomere lengths (SL) ranging from 2.0 to 2.2 µm, at which thin filament fully overlaps the A-band region of the thick filament bearing motors (Fig. 1.2). At larger SL, T_0 decreases in proportion to the increase of SL and of the I band region of the thin filament not overlapping with the thick filament.

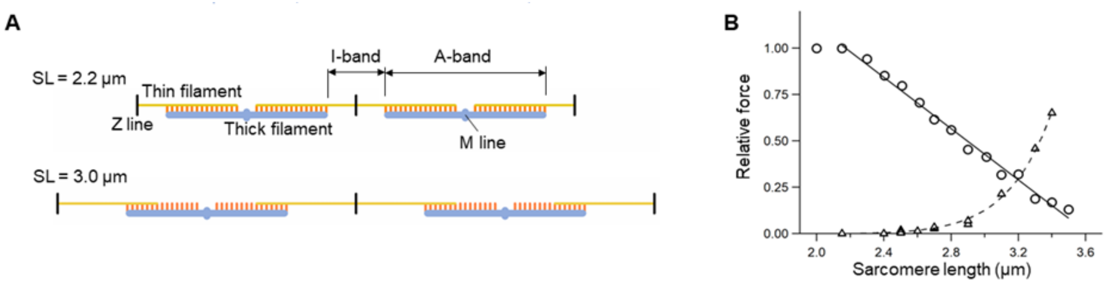

Figure 1.2. Schematic of the sarcomere at different sarcomere lengths and force-sarcomere length relation. A. Thick filament (blue), carrying myosin motors (orange), and thin filament (yellow) at SL 2.2 µm (full overlap) and 3.0 µm (partial overlap). Each sarcomere is bounded by the Z-line (vertical black line) and has the M-line, the thick filament midpoint, at its centre. As SL increases the overlap between filaments reduces, reducing the probability of myosin-actin interaction. **B.** Circles: relation between isometric tetanic force and SL in the range 2.0-3.5 µm. Triangles: passive force recorded in the same range of SL.

The half-sarcomere represents the basic functional unit in which the collective motor formed by myosin motors, the interdigitating actin filaments and other regulatory and cytoskeleton proteins (Fig. 1.3) accounts for the mechanical performance of muscle and its regulation.

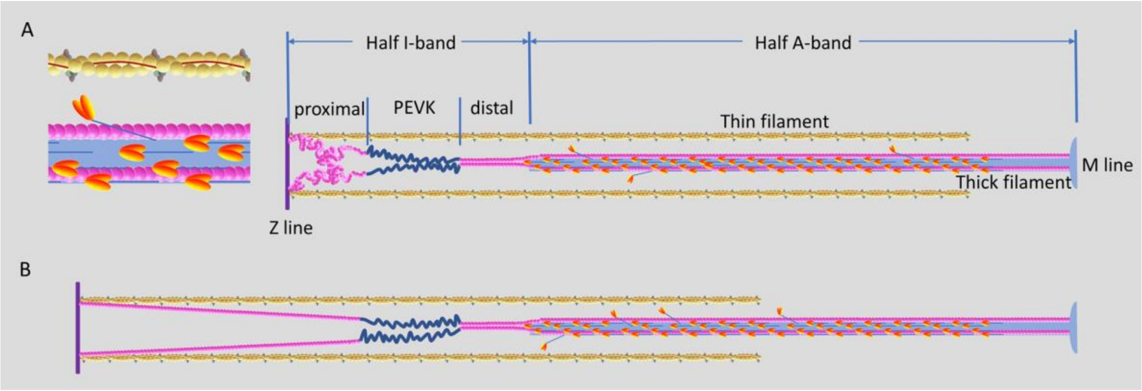

Figure 1.3. Layout of the proteins in the half-sarcomere at rest at 2.3 µm SL (A) and 3.0 µm SL (B). M-line on the right and Z-line on the left; violet, thick filament; yellow, actin monomers of thin filament; orange, myosin motors; brown, tropomyosin; gray, troponin complex; pink (Ig-domains) and blue (PEVK domain), titin (only two of the six titin molecules in the half-sarcomere are represented for simplicity). Inset: overlap region on an enlarged scale.

1.1.1 The sarcomere

Skeletal muscle is constituted by multinucleated cells, the muscle fibres, 30-200 µm in diameter, running the whole length of the muscle. Under the light microscope each muscle fibre appears striated because of the regular repeat of dark bands (A-bands, anisotropic under polarised light) and light bands (I-band, isotropic under polarised light) along the myofibrils, the cylindrical units of 1 µm diameter that constitute the fibre. Electron microscopy reveals that the bands are due to the regular repeat of two sets of interdigitating myofilaments (Fig. 1.1, A): the thin filaments, mainly formed by the protein actin (1 µm long, 8 nm in diameter) and the thick filaments mainly formed by the protein myosin (1.6 µm long, 12 nm in diameter).

The thin filaments originate from the Z-line, at the centre of the I-band and partially overlap to the thick filaments in the A-band. The sarcomere is the portion of myofibril delimited by two consecutive Z-lines. The part of thick filaments not overlapped with thin filaments appears paler and is called the H-zone. The electron dense line in the middle of the H-zone is the M-line, which contains proteins connecting the thick filaments together. Myosin motors emerge all along the thick filament except in a ~100 nm long zone on each side of the M-line called the bare zone.

In the cross section of the sarcomere (Fig. 1.1, B) thin and thick filaments appear disposed in a double hexagonal lattice: in the overlap region of A-band each thick filament is surrounded by six thin filaments, while each thin filament is surrounded by three thick filaments so that the ratio thick/thin filament is 1:2.

1.1.2 The contractile proteins and the myofilaments

Myosin and actin are the proteins responsible for muscle contraction and the two proteins together account for more than 70% of myofibrillar proteins (actin, 20%; myosin, 54%)(Hanson & Huxley, 1957; Huxley & Hanson, 1957). Striated muscle myosin belongs to the family of the myosin motor class II (Sellers, 1999).

The myosin molecule is an examer of 520 kDa molecular weight (Fig. 1.4, A) and consists of two heavy chains (220 kDa molecular weight) each composed of a 150 nm long ‘tail’ and a globular ‘head’ at one end, and two pairs of light chains (20 kDa molecular weight each). Partial digestion by trypsin splits the molecule in two fragments, the light meromyosin (LMM), constituted by the major part of the tail, and the heavy meromyosin (HMM) that contains the two heads and the rest of the tail. Further digestion by papain splits HMM into three sub fragments: two S1 portions, the heads, and a rod-like S2 portion. In the S2 portion the heavy chains form a coiled-coil structure which continues in the LMM that constitutes the backbone of the thick filament. The S1 portion of the myosin monomer (Fig. 1.4, B) consists of the catalytic domain (CD), or motor domain, containing the sites for actin binding and for ATP hydrolysis, and the light chain domain (LCD), an elongated portion that has the binding sites for the light chains (regulatory and essential) and is connected with its carboxyl terminal to the S2 rod. The primary structure of the HMM contains about 1900 amino acids of which about 840 form the S1 portion of the head.

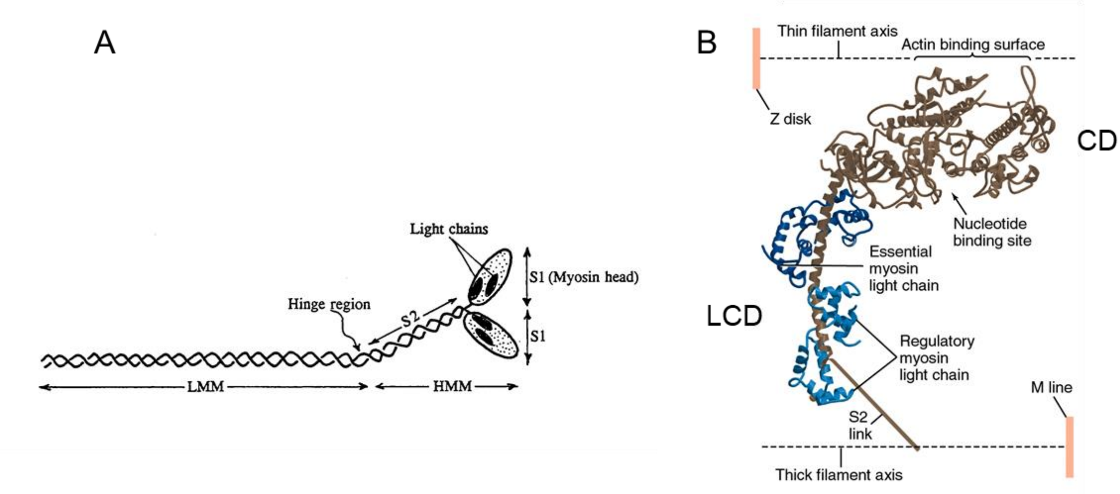

Figure 1.4. The myosin molecule. **A.** Schematic organization of the six polypeptide chains (two heavy chains and two pairs of light chains) in the dimer. Two globular portions (myosin head or S1) are attached to a long tail with a coiled coil structure, divided into an LMM section and an S2 section. S2 and the 2 S1 form the HMM section. **B.** Ribbon representation of the S1 crystallographic structure (Rayment *et al.*, 1993b). Brown: heavy chain with the catalityc domain CD, the globular part with the actin binding and nucleotide binding sites, and the light chain domain LCD, the elongated C-terminal or "neck" that carries two calmodulin-like light chains: the regulatory light chain (light blue) and the essential light chain (dark blue).

In the thick filament the myosin molecules are arranged in two antiparallel arrays, with the tails in each half of the thick filament pointing toward the centre of the sarcomere.

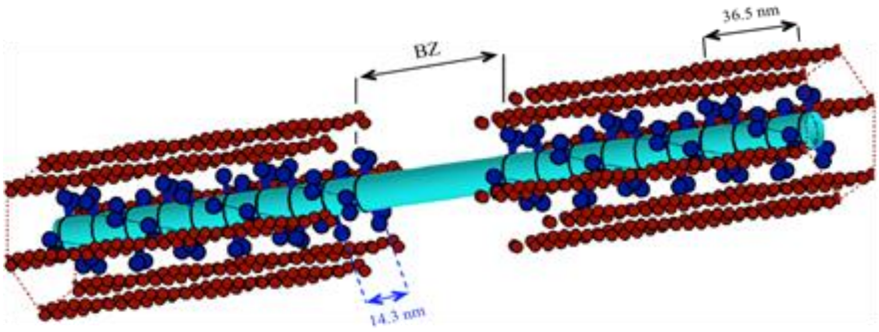

Figure 1.5. Schematic diagram of the organization of myosin (cyan and blue) and actin (red) in the myofilaments. One myosin filament is shown surrounded by six actin filaments. BZ, bare zone. Two periodicities are indicated: 14.3 nm, the axial repeat of myosin heads along the thick filament and 36.5 nm, the period of the actin helix in the thin filament.

Consequently, in the centre of the thick filaments, a region of ca 200 nm, called the bare zone (BZ), is free of heads (Fig. 1.5)The myosin filament is three-stranded and has a quasi-helical repeat distance of 42.9 nm. For each repeat there are three levels with axial repetition of 14.3 nm where three pairs of myosin heads project radially 120° apart. Each level is rotated 40° with respect to the next (Fig. 1.5). Each half-thick filament, 700 nm long, carries (700/14.3·6=) 294 myosin motors.

Electron microscopy and image analysis of thick filament allow to distinguish the two heads and the S2 portion (Woodhead *et al.*, 2005), revealing that the two heads in the relaxed state interact intramolecularly forming an asymmetric interacting-heads motif (IHM or J motif): one head (the blocked head) has its actin-binding site blocked by the interaction with the other head (the free head), which has its actin-binding domain freely exposed to interact with actin. The two heads in the J motif point in the direction towards the bare zone (Fig. 1.6).

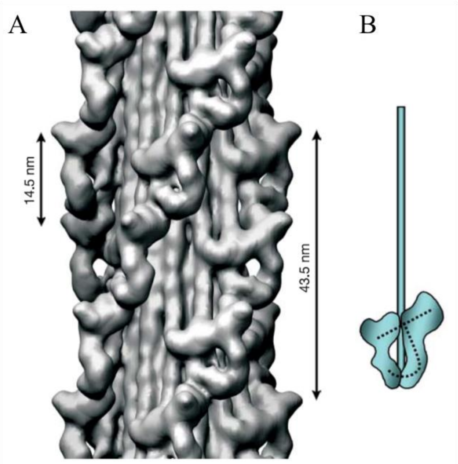

Figure 1.6. Surface view and 3D reconstruction of purified tarantula thick filament.
The repeating motif, representing a pair of myosin heads, has the appearance of a tilted J (B). Bare zone at the top. Modified from Fig. 1 of (Woodhead *et al.*, 2005).

The packing of the myosin heads on the surface of the thick filament has been associated with the biochemically defined super relaxed state in which myosin heads have a very low ATPase activity (Stewart *et al.*, 2010; Hooijman *et al.*, 2011). It has been suggested that the IHM is widely spread among different species and muscle types (Woodhead *et al.*, 2005; Zoghbi *et al.*, 2008; Pinto *et al.*, 2012) and has been conserved since invertebrates and vertebrates had diverged 600 million years ago (Peterson *et al.*, 2004; Jung *et al.*, 2008).

The actin filament (F-actin) is generated by the polimerization of G-actin monomers, a globular protein of 5.5 nm in diameter and 42 kDa molecular weight, in a one-start, left-handed helix. Because the rotation per monomer is large (166°) and there is extensive contact between alternate monomers, the actin filament appears as a two-stranded helix with period 36.5 nm (Fig. 1.5). Because the strands are half-staggered along the filament axis there is a monomer each (5.5 nm/2) 2.75 nm.

Two regulatory proteins, the troponin complex (Tn) and tropomyosin (Tm) are associated with the actin filament to form the thin filament (Fig. 1.3, A and 1.7, A). Tropomyosin is a filamentous dimer 40 nm long that polymerizes to form a filament lying in the groove between the two actin strands. The troponin complex, repeating every seven actin monomers for the entire length of the filament, consists of three subunits, troponin I that inhibits actomyosin ATPase activity, troponin C that binds Ca^2, and troponin T that binds to tropomyosin.

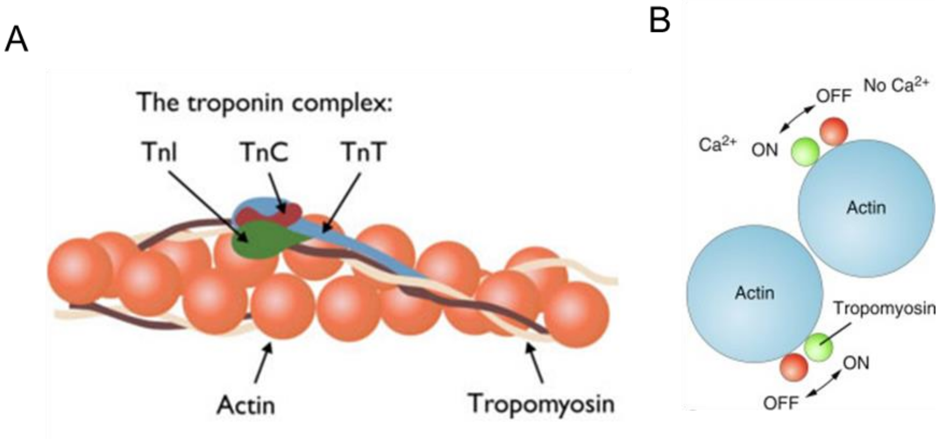

Figure 1.7. Schematic representation of thin filament based regulation. A. Structure of thin filament: orange, actin monomers organized in the two-stranded helix; brown and pale brown, tropomyosin; green, light blue and purple, respectively TnI, TnT and TnC subunits of the troponin complex. **B.** Steric block model of thin filament activation: upon Ca^{2+} increase Tm shifts from the OFF position (red) to the ON position (green) on the thin filament exposing the sites for myosin binding on the actin monomers (light blue).

1.2 Regulation of contraction

The contraction-relaxation cycle of the striated muscle is under the control of regulatory mechanisms in both the thick and thin filaments. The classical thin-filament-based activation mechanism provides that, following the rapid increase of intracellular Ca^{2+} concentration ($[Ca^{2+}]_i$) induced by the action potential, Ca^{2+} binding to troponin C triggers a series of structural changes in the Tn complex that lead to an azimuthal movement of tropomyosin around the filament surface that removes the steric inhibition of actin-myosin interaction making the actin sites available for binding of the myosin motors (Fig. 1.7, B) (Ebashi *et al.*, 1969; Huxley, 1973; Gordon *et al.*, 2000).

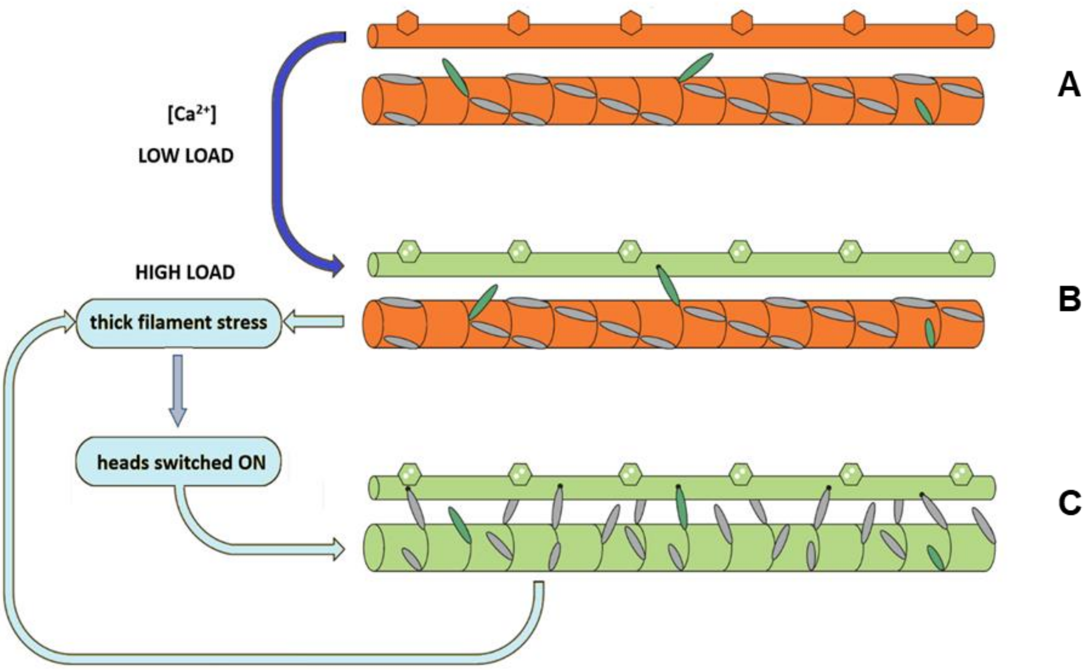

Figure 1.8. Scheme of the dual regulation of contraction of striated muscle. At rest, in the absence of calcium, both thin and thick filaments are in the OFF state. Myosin motors lie on the thick filament folded back towards the M-line. Increase of Ca^{2+} upon stimulation activates thin filament. As soon as thick filament is under stress, myosin motors switch ON causing further force production that, through a positive feed-back mechanism, induces further motor switching ON. In the scheme it is assumed that at rest some sentinel motors are constitutively ON so that as soon as the thin filament is activated, they attach to actin promoting the initial stress that activates the thick filament.

The need for a thick filament activation mechanism that makes myosin motors available for interaction with actin became evident following the structural evidence that the myosin motors in the resting state lie on the surface of the thick filament, folded back towards the centre of the sarcomere in the interacting heads motif, IHM, or OFF state (Fig. 1.6), unable to bind to actin (Woodhead *et al.*, 2005) and hydrolyses ATP (Stewart *et al.*, 2010) . By combining mechanics and X-ray diffraction on intact myocytes from vertebrate skeletal and cardiac muscle (Linari *et al.*, 2015; Reconditi *et al.*, 2017) it has been shown that myosin motors are recruited from their OFF state for attachment to actin by a mechano-sensing mechanism in the thick filament (Fig. 1.8).

The molecular basis of mechano-sensing, not yet defined in details, involves the interplay between the myosin motors, the regulatory protein myosin-binding protein C (MyBP-C) and the cytoskeletal protein titin on the surface of the thick filament (Fig. 1.3) (Herron *et al.*, 2001; Hidalgo & Granzier, 2013; Kumar *et al.*, 2015; Kampourakis *et al.*, 2016).

1.3 The cytoskeleton protein titin

Titin, called also connectin, is a giant protein (ca. 3000 kDa) that spans the whole half-sarcomere, connecting the Z-line at the end of the sarcomere with the tip of the myosin filament and then running, bound to the surface of the thick filament, up to the M-line at the center of the sarcomere (Maruyama *et al.*, 1977; Wang *et al.*, 1979); (Labeit & Kolmerer, 1995) (Fig. 1.3). There are six titin molecules per half-thick filament (Trinick, 1996). In the A-band titin forms specific periodic interactions with MyBP-C and myosin on the surface of the thick filament, since 11 domain super-repeats of titin match the 43-nm periodicity that characterises the axial repeat of the accessory protein MyBP-C and the helical repeat of myosin molecules (Rome *et al.*, 1973; Labeit *et al.*, 1992; Tonino *et al.*, 2019; Bennett *et al.*, 2020). This structural feature of A-band titin segment supports the idea of titin as the mechano-sensor in thick filament regulation. The I-band portion of titin comprises three distinct regions starting from the Z-line: the proximal tandem immunoglobulin(Ig)-like domain, the unique sequence rich in proline (P), glutamate (E), valine (V) and lysine (K) residues (PEVK domain) and the distal tandem-Ig domain (Labeit & Kolmerer, 1995). This three serially-linked, spring-like elements are responsible for the extensibility associated to the passive force developed when a skeletal muscle fibre is stretched, thus determining its passive stiffness (Furst *et al.*, 1988; Itoh *et al.*, 1988; Trombitas *et al.*, 1991; Anderson & Granzier, 2012). In this way titin assumes a unique function by providing a “third” elastic filament that links the end and the centre of the sarcomere and thus is able to transmit the stress also in the resting sarcomere, when no myosin motors are attached to actin.

In single muscle fibres, in which the contribution of the collagen from the extracellular matrix (ECM) is minimal (Meyer & Lieber, 2018), the spring elements in the I-band titin account for the passive force-sarcomere length (SL) relation (Fig. 1.2, B, triangles). In particular, since the distal Ig-domains, composed of the six titin molecules attaching to the tip of the thick filament (Bennett *et al.*, 1997), form a very stiff end-filament, the main contributors to titin elasticity are the proximal tandem-Ig-domain and the PEVK domain. Both domains exhibit variable muscle-type specific lengths depending on alternative splicing of the single titin gene (Labeit & Kolmerer, 1995; Freiburg *et al.*, 2000) and in this way determine the differences in passive force – SL relations between cardiac versus skeletal muscle and among different skeletal muscles (Neagoe *et al.*, 2003).

1.4 The role of titin in the passive and active sarcomere

In situ studies using immunofluorescence and immunoelectron microscopy of myofibrils of mammalian skeletal muscle have demonstrated how the different extensibility of the two I-band titin serially linked spring elements explain the shape of the passive force-SL relation (Fig. 1.2, B, triangles) (Linke *et al.*, 1996): the proximal Ig domains are responsible for the extensibility of the muscle sarcomere in the range of short SL (<2.7 μm). In this range the passive force is very small and the Ig domain portion accounts for sarcomere extensibility likely by straightening out of randomly bent elements from their collapsed state. PEVK domain is responsible for sarcomere extensibility at larger SL, at which passive force increases more steeply and the proximal Ig-domain spring has attained its contour length (Linke *et al.*, 1998a; Linke *et al.*, 1998b). Unfolding of individual Ig domains, a mechanism demonstrated in *in-vitro* mechanical experiments with single titin molecules and constructs (Kellermayer *et al.*, 1997; Rief *et al.*, 1997; Tskhovrebova *et al.*, 1997; Rivas-Pardo *et al.*, 2016), may occur *in-situ* at extreme further extension of the sarcomere (Granzier *et al.*, 1996; Linke *et al.*, 1996; Minajeva *et al.*, 2001). Titin provides the passive elasticity that maintains sarcomere structure (Horowits *et al.*, 1986; Horowits & Podolsky, 1987), but also supplies the sarcomere with a structural framework through association with other cytoskeletal and transmembrane proteins (Granzier & Labeit, 2002; Kontrogianni-Konstantopoulos & Bloch, 2003; Gautel & Djinovic-Carugo, 2016) and mediates mechanosensitive signalling processes by binding proteins responsible for sarcomere assembly and metabolism (Sorimachi *et al.*, 1995; Lange *et al.*, 2002; Ma & Wang, 2002).

Macroscopic production of power during contraction of striated muscle depends on maintenance of the ordered configuration of the contractile unit, the half-sarcomere, on different hierarchical levels, allowing summation of both shortening (and thus shortening velocity) through the serial arrangement of half-sarcomeres, and force by the packing of the myofilaments over the cell cross-section. The serial arrangement of thousands of half-sarcomeres provides a proportional amplification of the movement but, in the presence of a variability in the force generated by each in-series half-sarcomere, results in instability, especially under high load (Lombardi & Piazzesi, 1990). In fact, force equilibration within serially linked half-sarcomeres with an even small degree of variability in force production is attained with lengthening of the weaker half-sarcomeres caused by shortening of the stronger ones (Julian & Morgan, 1979). In the descending limb of the active force – SL relation (Fig. 1.2, B, circles), this phenomenon would cause progressive increase in sarcomere length inhomogeneity, which is limited only by the rising stress in the I-band titin spring. In fact in each half-sarcomere the I-band titin acts roughly as a spring in parallel with the array of myosin motors in the A-band (Pertici *et al.*, 2019), and the rising stress in the titin of weaker half-sarcomeres contributes to equilibrate the force of strong half-sarcomeres. However, passive force in a fibre starts to rise at SL >2.5 µm and attains levels comparable to active tetanic force at SL >>3 µm (Fig. 1.2, B) (Granzier & Wang, 1993; Reconditi *et al.*, 2014),indicating that the underlying static stiffness of titin is too low to prevent substantial lengthening of the weak sarcomeres.

I-band titin could exert an efficient role in preventing the development of sarcomere length inhomogeneity if its stiffness got much larger during contraction. A quantitative description of the I-band titin spring contribution *in situ* in the active half-sarcomere is hampered by the presence, in parallel with the I-band titin spring, of myosin motors with a stiffness one order of magnitude larger and rapid detachment/attachment kinetics (Lombardi & Piazzesi, 1990; Fusi *et al.*, 2014a; Powers *et al.*, 2020). Getting around these limits with mechanical protocols that imply extremely large SL to suppress the contribution of myosin motors does not provide physiologically reliable information.

Recently, with measurements of half-sarcomere stiffness by means of small 4 kHz oscillations imposed on single frog muscle fibres early during isometric force development, when the number of attached motors is small (Powers *et al.*, 2020) it was possible to characterise a titin-like I-band spring with an undamped stiffness two orders of magnitude larger than the static stiffness responsible for the passive force-SL relation. However, the viscoelastic properties associated to the structural dynamics of the I-band titin, that are the most relevant for their contribution to the contracting half-sarcomere and are qualitatively predictable by low time resolution *in-vitro* mechanics (Bianco *et al.*, 2007; Martonfalvi *et al.*, 2014; Rivas-Pardo *et al.*, 2016; Powers *et al.*, 2020), remained inaccessible.

1.5 Aims

The aim of this work is to define the function of I-band titin as a dynamic element in parallel with the array of myosin motors using fast half-sarcomere level mechanics on intact fibres of frog muscle in the presence of 20 μM para-nitro-blebbistatin (PNB) (Kovacs *et al.*, 2004; Limouze *et al.*, 2004), a drug able to inhibit thick filament activation and actin-myosin interaction. The use of single frog fibre is particularly suitable because this preparation exhibits an elasticity in parallel with the contractile elements that is free from the contribution of extra-cellular matrix (Magid & Law, 1985; Meyer & Lieber, 2018) and allows high resolution mechanical measurements on a population of sarcomeres selected near the force transducer in order to eliminate inertial effects in the kilohertz frequency domain (Fusi *et al.*, 2014a). Load dependent titin dynamics at different SL (range 2.3-3 μm) is determined at 4 and 14 °C by imposing 100 μs force steps (amplitude ΔT ranging from 0.12 to 0.4 $T_{0,c}$, the isometric tetanic force in control at 4 °C and SL 2.15 μm) at rest and during electrical stimulation at the frequency that in control induces maximal tetanic force by saturation of the intracellular [Ca^{2+}]. A force step perturbation is the most powerful tool to investigate the structural dynamics of molecular and intermolecular processes because, following the step, the force is kept constant so that the length response of the system is not influenced by any series compliance and directly records the molecular transformation under a constant potential energy landscape (Bianco *et al.*, 2014; Rivas-Pardo *et al.*, 2016).

1.6 Summary of results

Using X-ray diffraction from synchrotron light (European Sychrotron ESRF, Grenoble, France) we demonstrate that in the presence of 20 μM PNB myosin motors remain in their OFF state, in which they lie tilted backward along the surface of the thick filament independent of both electrical stimulation and thick filament stress. Under these conditions the half-sarcomere lengthening transient in response to a force step (0.12-0.4 $T_{0,c}$) is solely attributable to the dynamic response of the I-band titin. Microsecond information on the structural dynamics of the molecule is obtained by superimposing a small 4 kHz length oscillation throughout the response of the fibre to electrical stimulation and force perturbation.

We find that at rest the force step elicits a large fast lengthening, complete within a few tens of milliseconds, the amplitude of which progressively decreases at larger SL, a result that can be accounted for by the straightening of the proximal Ig domain region. On the contrary, during stimulation, the active response to the step consists in a much faster and smaller lengthening (more than one order of magnitude smaller at SL 2.3 μm), the amplitude of which underpins a stiffness of more than 3 pN/nm per half-thick filament (htf), which remains roughly constant in the whole range of SL studied. This indicates that the rise in internal [Ca^{2+}] switches titin I-band elasticity from its OFF compliant state to a stiff ON state through a process, likely the binding to actin of a segment of titin distal to the proximal Ig domain region, that substitutes the compliant proximal Ig segment with the stiffer actin segment and reduces the length of I-band titin spring to that of its distal portion, likely the PEVK domain. In this way, I-band titin in the ON state ensures the stability of serially linked half-sarcomeres during contraction at physiological SL as any stress undergone by a weaker half-sarcomere for the force excess of a stronger one will be equilibrated with a few % change in its length. 4 kHz oscillation analysis gives high resolution record of the time course of the OFF-ON switch of the I-band titin spring following the start of stimulation and its reversal after the end of stimulation. The time after the end of stimulation at which the recovery of the resting compliant viscoelasticity shows up is correlated to, and anticipates, the time at which, in the control tetanus recorded before PNB treatment, the relaxation switches from the slow isometric phase to the chaotic phase providing the necessary condition for the transition of tetanus to rapid relaxation. All the changes in titin mechanical properties with SL described above, either at rest or during stimulation, are the same when the measurements are repeated at a 10 °C higher temperature, proving that the mechanism has a structural rather than a kinetic basis, whereas the time courses of all the transitions become two-three times faster at the higher temperature, in agreement with the reported timing and temperature sensitivity of the Ca^{2+} transient elicited by the action potential and the ensuing thin filament activation. The strict time sequence of these events suggests that the rate limiting step for the binding of titin to actin that switches the titin I-band spring ON is the same structural change in the thin filament that makes actin sites available for the interaction with myosin motors.

Chapter 2. Methods

2.1 Preparation and mounting of the fibre

2.1.1 Muscle fibre preparation

The experiments were done on single muscle fibres or small fibre bundles (3-4 fibres each) from *Rana esculenta*, isolated from the lateral head of the tibialis anterior (single fibres) or lumbricalis (fibre bundles) muscle. Single fibres had a cross-sectional area (CSA) of 6000-12000 μm^2, suitable for sarcomere mechanics because of the high level of sarcomere homogeneity along and across the fibre. Fibre bundles were prepared for X-ray diffraction experiments to have a larger total CSA that allowed a larger signal-to-noise ratio in the collected X-ray diffraction patterns.

Frogs were kept in humid cases at 4-7 °C and killed by decapitation followed by the destruction of the spinal cord in agreement with the Authorization 956/2015-PR in compliance with Decreto Legislativo 26/2014 and with EU directive 2010/63. Fibre dissection was performed under a stereomicroscope (Stemi SV6 or SteREO Discovery V8, Zeiss) with the aid of small knives, tweezers and scissors, in a Perspex trough containing Ringer solution, at room temperature. Dark-field illumination was used during the dissection. Special care was taken in dissecting and mounting the muscle fibre in order to minimize the amount of passive compliance in series with the sarcomeres and transverse movements of the fibre during contraction or imposed length/force changes. Fibre tendons were trimmed to a length as short as possible (total length around 300 µm), and held with aluminium foil clips (Ford *et al.*, 1977).

2.1.2 Mounting of the fibre for mechanical experiments

The fibre was horizontally mounted in a thermoregulated aluminium trough between the lever arms of a force transducer and a loudspeaker motor (Fig. 2.1) by means of the aluminium clips that allowed to obtain an optimal alignment between the fibre and the transducer and motor levers. The bottom of the trough (in which a channel of the proper dimensions was drilled in order to illuminate the fibre) and its internal walls were covered by pieces of microscope cover-glass to electrically insulate the bath.

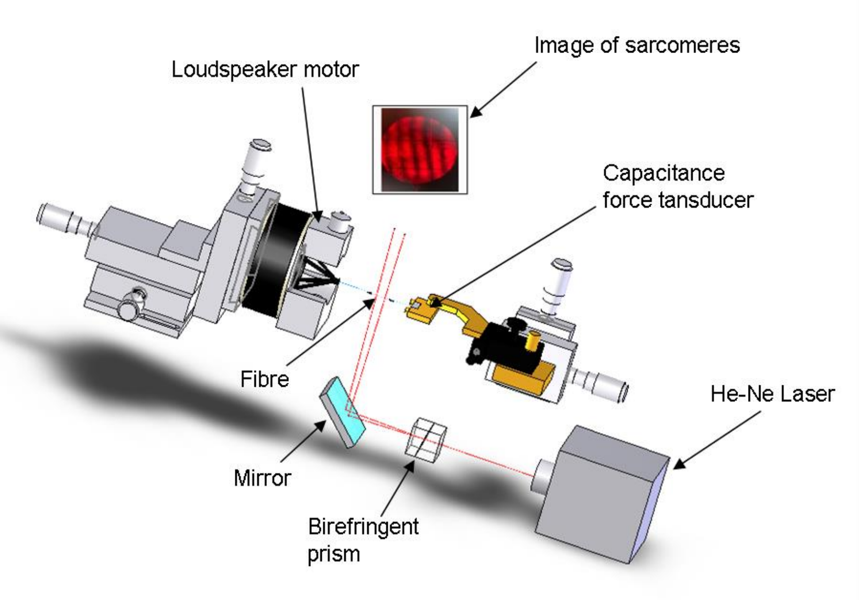

Figure 2.1. Mechanical setup for half-sarcomere mechanics. Muscle fibre is mounted between the levers of a loudspeaker motor (left) and a capacitance force transducer (right). Half-sarcomere length is monitored by means of a striation follower. A He-Ne laser beam is split by the birefringent prism into two beams focused on the fibre. The diffracted beams are collected by the optics of the striation follower giving an image of the sarcomeres as a sinusoidal intensity distribution of light.

The top of the trough was covered with a cover-glass carrying two platinum plates electrodes running parallel to the fibre. The position of the fibre in the trough and its resting length were adjusted by means of two micromanipulators carrying the force transducer and the loudspeaker motor. During the experiment the temperature in the trough (4 or 14 °C) was continuously monitored with a thermistor that provided the feedback signal for the temperature control circuit, the output of which fed a thermoelectric module stuck to the bottom of the experimental chamber. The whole system (experimental trough, loudspeaker motor, force transducer) was carried on a metal plate connected to the movable stage of an ACM microscope stand (Zeiss).

2.2 Fibre measurements

Measurements were made under ordinary light on the movable stage of the ACM microscope using a 40x water immersion objective (Zeiss) and a 25x eyepiece. Striation spacing was determined by averaging, at different points along the fibre (~ 500 μm apart), the number of sarcomeres in twenty divisions of the graduate scale of the 25x eyepiece that correspond to (20 div · 2.04 μm/div=) 40.8 μm. Fibre length was determined by means of a dial gauge mounted on the stand of the ACM microscope, by measuring the displacement of the movable stage in the direction of the fibre axis required to move the two tendon ends of the fibre to the centre of the microscope optic field. Fibre length was initially adjusted to have an average sarcomere length (SL) along the fibre of 2.15 µm. At the same points at which SL was measured, the height (*h*) and the width (*w*) of the fibre were determined and the fibre CSA was calculated as if the section were elliptical (A= $w \cdot h \cdot \pi/4$). The height was determined with the fine focusing motion at the middle of the fibre width. The width was read on the graduated scale of the eyepiece.

2.3 Fibre stimulation

Stimuli of alternate polarity were applied transversely to the muscle fibre by means of electrodes across which up to 10 V could be applied with a constant-voltage pulse generator. Stimuli of 1.5 times the threshold and 0.5 ms duration were used. Tetanic stimulation was applied in volleys of even numbers of stimuli, so that the first stimulus of each tetanus always had the same polarity. The optimal stimulation frequency was the minimum frequency for a fused tetanus and was determined for each fibre at 4 °C (18-25 Hz) and 14 °C (50 - 60 Hz).

2.4 Solutions

The physiological solution (Ringer) had the following composition: 115 mM NaCl, 2.5 mM KCl, 1.8 mM $CaCl_2$, 3 mM phosphate buffer at pH= 7.1. Para-nitroblebbistatin, PNB, (supplied by Prof. András Málnási Csizmadia) was dissolved in dimethyl sulfoxide (stock solution, 13 mM concentration) and added to the Ringer’s solution to have a final concentration of 20 µM.

2.5 Mechanical Setup

2.5.1 Force transducer

Tension (kN/m^2 = kPa) was measured by means of a capacitance force transducer similar to that described by Huxley and Lombardi (1980).

The transducer is composed of two fused quartz plates (one fixed and one mobile), metallized with gold deposition on the facing sides, that form a capacitor. Part of the metallization on the fixed plate is removed so as to isolate the central area used as the live electrode. The mobile plate is kept at 6-10 µm from the fixed one by interposition of gold foils (Fig. 2.2) which also provide electrical connection to the metallization on the moving plate. The force produced by the muscle fibre is directly applied to the centre of the moving plate by means of a glass lever hook (3-5 mm of length, 100-125 µm of diameter) attached to it. The bending of the moving plate, caused by the applied force, changes the air gap between the conducting surfaces of the two plates and thus the capacitance of the transducer. Capacitance changes are detected with a phase-discriminator circuit (Cambridge & Haines, 1959; Cecchi, 1983). With this circuit the sensitivity of the force transducer ranges from 50 to 250 mV/mN and the noise from 2 to 10 mV peak to peak (Huxley & Lombardi, 1980). The sensitivity of the force transducers used here ranged from 50 to 120 mV/mN, the noise from 2 to 8 mV peak to peak and the resonance frequency from 30 to 50 kHz. In force clamp experiments, the output of the force transducer was used as the feedback signal to the servo-control system of the motor position.

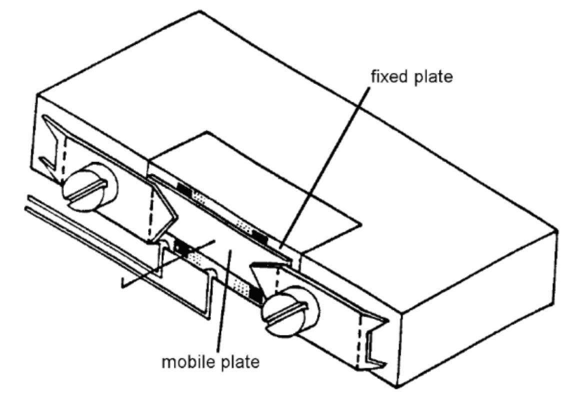

Figure 2.2. Force transducer

2.5.2. Loudspeaker motor

Step and sinewave length changes were imposed on the muscle fibre by means of a loudspeaker coil motor (Fig. 2.3) similar to that described by Lombardi and Piazzesi (1990). The loudspeaker cone is removed and substituted by a pyramidal structure in carbon fibre directly stuck to the coil. A stainless steel lever is glued on the top of the pyramid with a hook at its distal end. The mobile part of the loudspeaker is anchored to the fixed one by means of elastic connections. For recording the lever movement a bulb and two photodiodes are mounted on two aluminium plates, fixed one in front of the other on the loudspeaker iron plate and a flag is glued between the two pyramid pillars in front of the photodiodes. This flag partially cuts off the light beam directed to the photodiodes so that the movement of the coil and of the pyramid produces proportional changes in their illumination. The two photodiodes are differentially connected in order to double the sensitivity and remove the effects of diffused light. The position of the motor lever is servo-controlled by a feedback circuit in which the feedback signal is the output of the photodiodes (fixed-end mode), or the output of the force transducer (force-clamp mode). In fixed-end mode, the control signal to be compared with the output of the photodiodes is either zero (isometric condition) or a step or/and sinewave that change the position of the lever and thus the length of the fibre. In force-clamp mode the control signal (to be compared with the output of the force transducer) is set to a value corresponding to a fraction of the isometric plateau force: the position of the motor lever changes so that the selected force is maintained for the whole duration of the clamp.

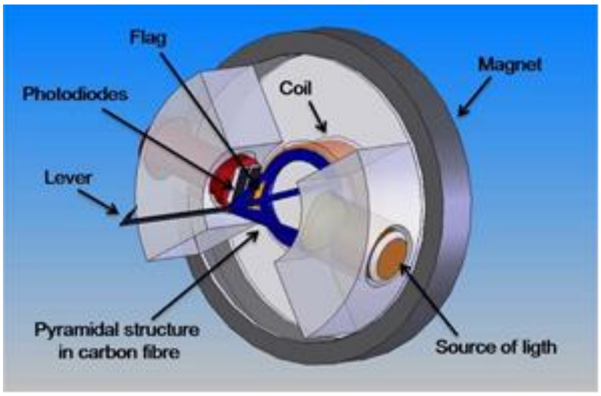

Figure 2.3. Loudspeaker motor

In the experiments described here, the sensitivity of the signal coming from the photodiodes was set to ~20 mV/µm of displacement of the lever. Step displacements of the loudspeaker lever arm up to 100 µm were complete within about 100 µs. The maximum linear displacement of the motor coil was about ± 600 µm. In force-clamp experiments the force was stepped to a value ranging between 0.12 and 0.4 the maximum isometric force T_0 developed during a tetanus at 2.15 µm SL at 4 °C ($T_{0,c}$).

2.5.3. Striation follower

This apparatus is an optoelectronic device similar to that described by Huxley and collaborators (Huxley *et al.*, 1981). It is composed of a light source (a 5 mW He-Ne laser, ThorLabs, Newton, New Jersey), a modified microscope mounted on the ACM stand and two photodiode arrays feeding analogue and digital electronics. The instrument measures the longitudinal displacement of two distinct regions along the fibre, each about 10 µm broad and containing six consecutive sarcomeres. The distance between these two regions is adjusted to 0.5-3 mm by rotating a birefringent prism that splits the laser beam in two beams that are focused to form two spots of about 10 µm diameter.

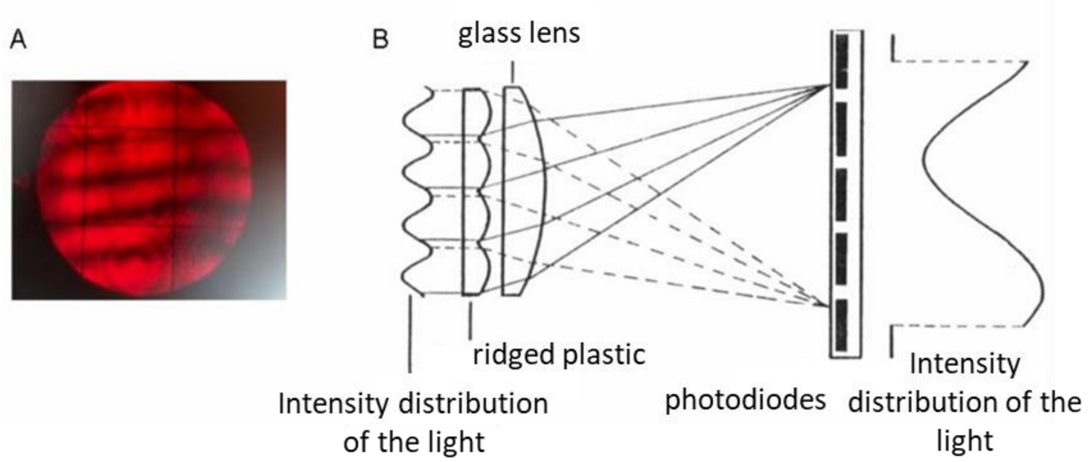

Figure 2.4. Striation_follower. A. Image of the sarcomeres from one of the two regions at the level of the photodiode array. **B.** System for obtaining the optic average of the intensity distribution of several sarcomeres.

The angle of incidence of the illuminating beam is offset from the normal to the fibre axis so that the zero-order and only one first-order diffracted beam from each spot are collected by a 10x objective giving a simplified image of the sarcomeres represented by a sinusoidal intensity distribution of light (Fig. 2.4). This distribution (magnified 2000x) is projected, via a collimator and a projector, onto a plate with 6 cylindrical lenses mounted on the ACM stand, the height of which can be changed to have a magnification adjusted to a sarcomere per cylindrical lens. The adjustment is obtained by controlling the magnification with a 10x eyepiece (Zeiss, Germany), receiving part of the light distribution from a partially reflective prism, placed before the cylindrical lenses, that projects the image on a calibrated grid placed at the same distance as the lenses. The light distributions of the sarcomeres produced by cylindrical lenses are superposed with a convergent lens, forming a single light distribution representing the optical mean of the images of the six sarcomeres. This distribution is projected onto an array of five photodiodes, ranging from half the first to half the fifth (Fig. 2.4, B). The current signals from the 5 photodiodes (I_1-I_5) are combined to give two output signals ($x=I_1 + I_5 - I_3$ and $y=I_2 - I_4$) sensitive to the sinusoidal intensity distribution of the light due to the sarcomeres and not to the intensity of the diffused light. The longitudinal movement of the fibre produces a variation of the intensity distribution given by $x = A\cdot\cos(2\pi\cdot D/SL)$ and $y = A\cdot\sin(2\pi\cdot D/SL$, where D is the fibre displacement and SL the average sarcomere length. The two signals from the photodiode arrays feed analogue and digital electronics giving an output signal that measures the displacement of the region of the fibre in terms of sarcomere length with a precision of about 1% of the striation spacing and a time response of 1 µs, over a range of 128 sarcomeres.

The sarcomere displacements occurring at the level of the two regions are subtracted from each other so that the output signal gives the actual length change undergone by the selected fibre segment. The signal is converted into nm per half-sarcomere on the basis of the number of half-sarcomeres in the segment. Thus the error in the measurement of average length change per half-sarcomere is reduced by a factor corresponding to the number of half-sarcomeres in the segment. The sensitivity is adjusted to 100 mV/nm per half-sarcomere.

Systematic errors may result from inhomogeneity of the sarcomere length within the segment and from changes of the sarcomere length in the laser spots upon activation. The sarcomere inhomogeneity of the fibres used here was less than 5% at rest and those fibres developing gross inhomogeneities upon activation were discarded.

2.6 Mechanical Protocol

The fibre was electrically stimulated to develop fused tetani at 4 min intervals at 4 °C and 14 °C, using trains of stimuli (train duration ~300 ms at 4 °C and ~260 ms at 14 °C) at different SL (2.15, 2.3, 2.5, 2.7 µm). Temperature and SL were randomly changed in different experiments. A force step of about 0.2 the isometric force determined at 4 °C at 2.15 µm SL ($T_{0,c}$) was imposed at rest at 2.7 µm SL to elicit an isotonic lengthening transient in control conditions at the two temperatures. Temperature was then set to 14 °C and the fibre perfused with Ringer solution containing 20 µM PNB. The fibre was stimulated every 5 min to control the progression of the effect of PNB that took 30-40 minutes to be completed: upon stimulation there was no sign of force development neither the striation follower detected any change of sarcomere length. At the two temperatures (4 and 14 °C), isotonic lengthening transients were elicited at different sarcomere lengths (2.3, 2.5, 2.7 and 3.0 µm), both at rest and during tetanic stimulation, by applying to the fibre a force step to 0.12-0.4 $T_{0,c}$ (that is to 0.12-0.4 the isometric force determined at 4 °C at 2.15 µm SL in the control solution) complete in 100 µs. At each temperature stimulation frequency was the same as that used in the control and the force step was imposed 60 ms following the stimulus start. In fig. 2.5 the lengthening response to a 0.2 $T_{0,c}$ step (upper trace) imposed either in control (Rest) or during tetanic stimulation in the presence of PNB (Active) is shown. The transient is composed of an initial phase, phase 1, simultaneous with the force step, followed by a quasi-exponential lengthening, phase 2, much larger at rest than during stimulation, that continues in a slow lengthening at constant velocity, phase 3. . Given the speed of phase 2 and the relatively slow step in force feedback (200-300 μs duration), phase 1 merges with the initial part phase 2. In the active transient, following the end of stimulation, the velocity of phase 3 increases again, indicating the recovery of the resting conditions (phase 4).

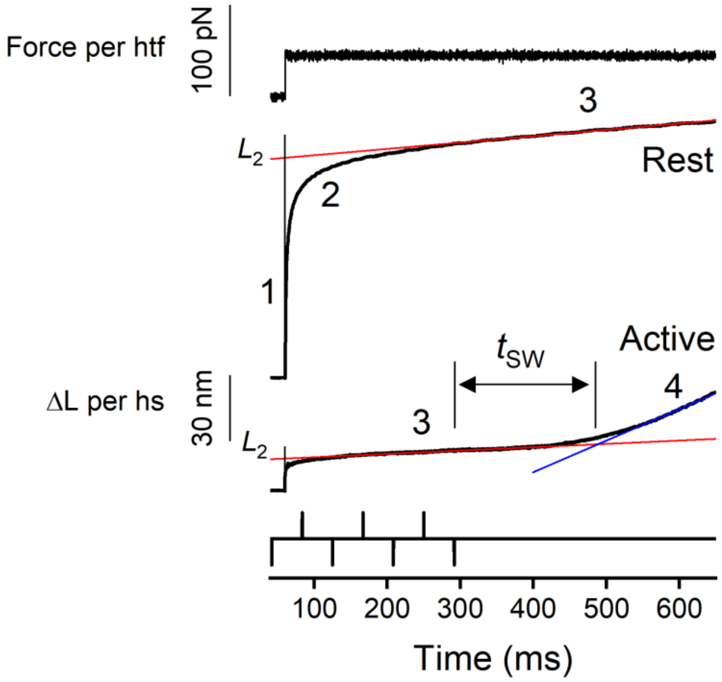

Fig. 2.5. Sample records of the lengthening response to a force step (upper panel) in control (Rest) and during stimulation in PNB (Active). L_2 indicates the amplitude of lengthening attained in phase 2, estimated by extrapolating back to half-time of the step the tangent to the linear part of phase 3 of the transient (red lines). t_{sw} is the difference between the time when lengthening velocity starts to increase (the intersection between red and blue line) and the time of the last stimulus. Bottom panel: stimulation frequency.

The instantaneous stiffness (e_1) of the half-sarcomere (hs) before and during the lengthening transient both at rest and during tetanic stimulation was estimated at 3.0 μm sarcomere length from the changes of the force and half-sarcomere length detected by the striation follower in response to 4 kHz longitudinal oscillations imposed throughout the record (see Fig. 3.6). Ten cycles of ~ 1.5 nm per hs peak-to-peak oscillations were applied and repeated at 2 ms intervals for the first 200 ms of the record and then at 40 ms intervals in the following 400 ms (at 14 °C) and 500 ms (at 4 °C) (Fig. 3.6). As first reported by Fusi *et al*. (2014) and Powers *et al*. (2020) with a 4 kHz oscillation the inertial effect due to the acceleration of the fibre mass at the loudspeaker-motor end is responsible for a phase lag ($\varphi < 0$) observed at low forces between the force and the motor position (the input oscillation). However, the distribution of the mechanical perturbation along the fibre (Cecchi *et al.*, 1987) implies that the acceleration and thus its inertial effect progressively reduce approaching the force transducer end of the fibre. To minimize the phase lag due to the inertial effect, the length change recording from the striation follower was from a segment selected close to the force transducer.

The different amplitudes of the force steps and the different sarcomere lengths were set in a random sequence (with the exception of 3 μm, which often (in four out of the eight fibres used for these experiments) was saved for the end of the experiment due to a higher risk of irreversible effects on the sarcomere structure)

2.7 Mechanical data collection and analysis

Force, motor position and sarcomere length signals were recorded with a multifunction I/O board (PXIE-6358, National Instruments). A program written in LabVIEW (National Instrument) was used for signal generation and data acquisition. Data analysis was performed using Excel (Microsoft), OriginPro 8.0 (OriginLab Corporation) and programs written in LabVIEW.

The amplitude of the lengthening response to a force step at the end of phase 2, $L_{2,}$ was estimated by extrapolating back to the half-time of the step (vertical black lines in Fig. 2.5) the tangent to the linear part of the transient (red lines). The time at which, following the end of stimulation, the lengthening velocity during the force step starts to increase (t_{sw}) is measured as the difference between the time at the intersection of the tangent to phase 3 (red line in Fig. 2.5) with that to phase 4 (blue line) and the time of the last stimulus. The parameters force (pN) and half-sarcomere stiffness (pN/nm) have been determined per half thick filament (htf), considering a density of thick filaments per CSA of $5.87*10^{14}$ m^{-2} (Appendix A in (Barclay *et al.*, 2010)).

The Fourier transform of the force (T, pN per htf) and length (L, nm per hs) traces (Fig. 3.6) during oscillations was calculated to extract the in-phase component and the out-of-phase components of the response. Traces were filtered before applying the

Fourier transform by applying a band filter (2 kHz-6 kHz) of the 4th order. The in-phase component was used to determine the elastic modulus, e_1 (pN/nm per htf). The phase shift (deg) is defined as the difference between the phase of T and that of L and its positive value indicates the viscous nature of the out-of phase component.

The time course of the increase of e_1 following the start of stimulation and of its drop following the last stimulus is fitted by the sigmoidal equation $e_1 = a + \frac{(b-a)\times t^n}{k^n + t^n}$. where *a* and *b* are respectively the start and end points of the sigmoid, k the time at which e_1=0.5×(b-a) and *n* the Hill coefficient, related to the slope of the relation.

Data are expressed as means ± SEM. Data are from 8 fibres in total. Given the complexity of the experimental design (combination of force steps of different sizes at different SL and different temperature and 4 kHz oscillations) not all the fibres contributed to the different protocols. The number of fibres contributing to each protocol is reported along the text and in the figure legends. The values of n reported in Tables 3.1-3.3 refer to the total number of repeats for each test, and consequently it can be larger than 8. As regards the parameters reported in Table 3.4 referring to 4 kHz oscillation analysis, they were obtained from 4 fibres by averaging different numbers of oscillations as indicated by n. The big variation among n's reflects the different time intervals during which averaging is done as reported in Table legend.

2.8 X-ray diffraction setup

The X-ray diffraction experiments have been performed at the high brilliance ID02 beamline of the European Synchrotron Radiation Facility (ESRF, Grenoble, France), a third generation X-ray source with low electron beam emittance and high photon flux. The fibre bundle was mounted in a thermoregulated trough adapted for X-ray measurements (Fig. 2.6). Two hollow cylinders carrying two mica windows and the stimulating electrodes (made of platinum wires stuck on the upper and lower surface of the window) were moved as close as possible to the fibre, to minimize the X-ray path through the solution.

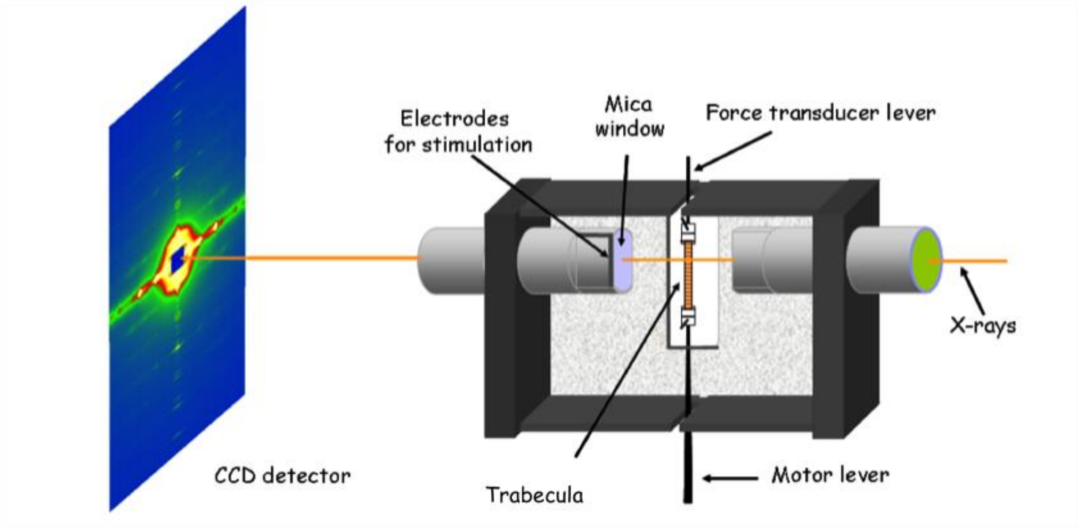

Figure. 2.6. Scheme of the vertical mounting of setup at the synchrotron beamline

The gap between the windows was typically 600 µm. A Perspex cover, adapted to the upper profile of the trough, was then sealed with silicone grease, to prevent the leakage of the physiological solution when the plate carrying the trough, micromanipulators, loudspeaker motor and force transducer was mounted vertically on a holder in the beam path, with the force transducer on the top and the motor at the bottom (Fig. 2.6). The vertical mounting of the trough is necessary to match the fibre axis to the smaller (vertical) size of the X-ray beam and maximize the spatial resolution of X-ray signals along the so-called meridional axis, parallel to the fibre axis.

2.8.1 Beamline characteristics

The beamline ID02 of the ESRF is dedicated to X-ray Scattering techniques: Small-Angle (SAXS), Wide-Angle (WAXS) and Ultra-Small-Angle (USAXS). Two undulators in series provide an X-ray beam with high photon flux and low divergence. Each undulator consists in a periodic repeat of dipole magnets inserted in the straight path of the electron beam. The electrons traversing the periodic magnet structure undergo oscillations and emit radiation that adds up at every oscillation, resulting in a beam with a higher flux and concentrated in a narrow angular range at a wavelength that depends on the repeat length of the magnets. The beam is highly collimated and its size is about the same at the sample and at the detector. During the visits for the experiments described here it was ~ 300 µm x 50 µm (horizontal x vertical, Full Width at Half Maximum, FWHM), with a flux of 10^{13} photons/s at a wavelength of ~0.1 nm. Two fast electromagnetic shutters in series (tandem shutters) were used to limit the X-ray exposure times to the data collection period, in order to minimise the radiation damage

2.8.2. The FReLoN CCD-based detector

Diffraction patterns were collected on a CCD (Charge Coupled Device) detector, a highly sensitive photon detector, formed by a 2D array of sensitive elements (pixels) built onto a silicon chip. When a photon of light falls within one of the pixels it is converted into one (or more) electrons and the number of electrons collected is directly proportional to the number of photons. The FReLoN (Fast Read out Low-noise) detector developed at the ESRF is based on a CCD coupled with a phosphor screen that converts X-rays into visible light. The active area is 50×50 mm^2 with 2048×2048 pixels and a point spread function (PSF, mainly determined by the phosphor screen) of about 80 μm (FWHM). The effective gain of the system is optimized to obtain the single photon level above the readout noise (the main noise source) of the CCD.

In the experiments described here 8 adjacent pixels along the equatorial direction (perpendicular to the fibre axis) were read as one (8x binning) to reduce the overall readout noise and increase the signal to noise (S/N) ratio without affecting the spatial resolution along the meridional direction (parallel to the fibre axis)

2.8.3 Signal generation and acquisition

Tandem shutter opening and CCD data acquisition were synchronised with the timing of the mechanical protocols by using the same LabVIEW program used for mechanical experiments. The intensity of the beam hitting the sample and the time windows of exposure were recorded by using a pindiode, which collects a small fraction of the primary beam scattered by a scattering foil, located within the X-ray pipe between the shutter and the sample.

2.9 X-ray diffraction acquisition protocol

Given the long time for PNB to fully inhibit force development (30-40 min), it was not viable to collect data in control Ringer solution and in PNB Ringer solution from the same fibre bundle because radiation damage going on from the first exposure would have affected the response. Thus control experiments were carried on preparations different from those treated with PNB. In both cases the beam was attenuated for bundle alignment and the trough was vertically translated by 100-200 μm between exposures to spread the X-rays over the sample and reduce radiation damage.

In control experiments 2D diffraction patterns were first collected with 5 ms time windows at rest and at the plateau of the isometric tetanus at 4 °C, at 2.15 μm and 2.7 μm SL. Then a 0.25 $T_{0,c}$ force step was imposed at rest at 2.7 μm SL and patterns were collected 10 ms before the step and 50 ms after the step. In PNB experiments, before starting the perfusion with PNB, the fibre bundle was mounted in Ringer solution and tetanically stimulated at 4 °C and 2.15 μm SL in order to record the reference $T_{0,c}$. Then the bundle was perfused with PNB Ringer, the trough was sealed and mounted in the X-ray beam. 2D diffraction patterns were collected at 2.15 and 2.7 μm SL, at 4 °C, with 5 ms time frames at rest and during tetanic stimulation at the same frequency as that used to record the control tetanus at 2.15 μm SL. A force step of 0.25 $T_{0,c}$ was imposed on the fibre bundle both at rest and 60 ms after the first stimulus of tetanic stimulation and 2D patterns in 5 ms time windows were collected 10 ms before the step and 50 ms (rest) or 2 ms (stimulated) after the step. The different timing of the X-ray windows at rest and during stimulation was chosen to take into account the much faster speed at which the lengthening transient occurs during stimulation.

2.10 X-ray diffraction data analysis

The 2D X-ray patterns recorded during the experiments were automatically corrected on-line for dark subtraction (that is removal of basal level of noise), flat field (normalization by the different pixels sensitivity of the detector) and spatial distortion of the detector.

The off line analysis of X-ray data was performed in the laboratory in Florence using the Fit2D software (Hammersely, ESRF) and IgorPro (WaveMetrix Inc.).

Single 2D patterns were shifted and rotated to have the four quadrants symmetric relative to the centre of the image patterns using the equatorial 1,0 reflection, then quadrant folded (mirrored) to enhance the signal-to-noise ratio.

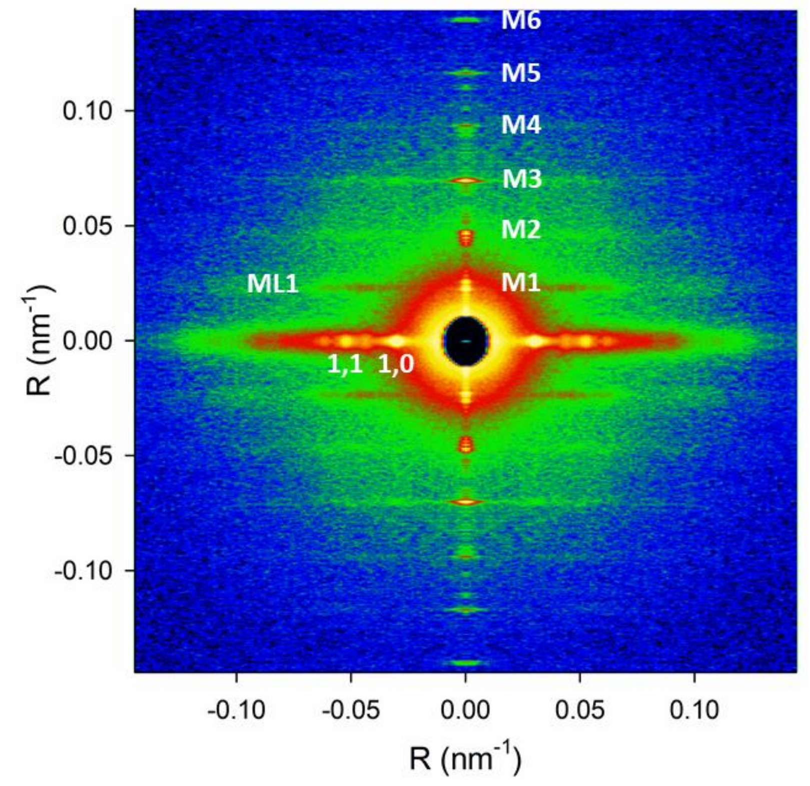

Figure 2.7. 2D pattern collected from a single muscle fibre at rest in PNB Ringer with a 1.6 m camera length. SL 2.7 µm, temperature 4 °C . Exposure time 10 ms. The vertical axis corresponds to the fibre axis.

Fig. 2.7 shows a typical pattern at rest following mirroring. The vertical axis, parallel to the fibre axis, is called the meridian and the reflections along it are the meridional reflections. Those indexed M1 to M6 are orders of a fundamental axial periodicity of ca. 43 nm, associated with myosin. Among them, the M3 reflection from the axial repeat of myosin motors has a periodicity of 14.34 nm, and M6, dominated by the periodic mass distribution in the thick filament backbone has a periodicity of 7.17 nm; M1 (which is also contributed from MyBP-C), M2, M4 and M5, the so-called forbidden reflections, signal systematic perturbations of the arrangement of myosin motors on the thick filament. The reflections along the equatorial axis are due to the crystallographic planes originating from the regular disposition of the myofilaments in the lattice. Among them, the most intense are the so-called 1,0 (mainly from the thick filaments) and the 1,1 (from both thick and thin filaments). The off-meridional layer lines parallel to the equatorial axis originate from structures with helicoidal symmetry. Among them, the first myosin layer line reflection at ~43 nm (ML1), is due to the three stranded helical symmetry of the myosin motors on the surface of the thick filament.

This 2D pattern is the signature of the OFF state of the myosin motors.

The 2D patterns were integrated along the meridian or equatorial axis to get 1D intensity profiles (see fig. 3.1) for further analysis. The distribution of the diffracted intensity along the meridional axis was calculated by integrating 0.0046 nm^{-1} (30 pixels) on either side of the meridian for measuring the spacing of the reflections and 0.012 nm^{-1} (80 pixels) for measuring their intensity. The narrower integration limits were chosen in order to have a better definition of the spacing and fine structure of the reflection, with an optimal signal-to-noise ratio. On the other hand, the larger integration limits are necessary to o include the whole intensity of the reflection in the measure. The ML1 reflection was integrated in the region between 0.064 and 0.037 nm^{-1} (180 pixel wide) from the meridional axis. The distribution of diffracted intensity along the equatorial axis was calculated by integrating 0.0036 nm^{-1} (24 pixels) on either side of the equator.

In the 1D patterns the reflections emerge from a background due to the diffuse scattering from the solution and disordered material present in the preparation. The background intensity distribution was determined using a *convex hull algorithm* and subtracted. The 1D intensity profiles of the reflections (with the exception of ML1) were fitted with a Gaussian peak (1,0 and 1,1, integration limits 0.029-0.041 nm^{-1} and 0.052-0.070 nm^{-1}, respectively) or multiple Gaussian peaks with the same axial width (M3 and M6, integration limits 0.067-0.072 nm^{-1} and 0.133-0.144 nm^{-1}, respectively). The total intensity of a reflection was calculated as the sum of the component peaks and its spacing was determined from the weighted mean of the centres of the component peaks, calibrated using as a reference the position of the M3 reflection in the fibre at rest at full overlap (sarcomere length 2.1-2.2 μm), taken as 14.34 nm (or 0.069735 nm^{-1} in reciprocal spacing).

The intensity of ML1 reflection was obtained by integrating 1D distribution between 0.019–0.023 nm^{-1} corresponding to the half, low angle side of the reflection to avoid contamination with the overlapping, non-resolved AL1 layer line from the actin helix ((Piazzesi *et al.*, 1999)).

Fibre activation or an applied external force may induce loss of register between myofilaments that causes a radial spread of the meridional reflections across the meridional axis and affects their intensities. To correct for this effect the intensity of the M3 reflection was multiplied by its radial, cross-meridional width determined from

Gaussian fits of the integrated radial intensity distribution in the axial region defined above.

The observed intensity of the reflection is influenced by the mass of the fibre under the X-ray beam, which depends on its CSA and on possible inhomogeneities along the fibre. It also varies with inverse proportionality to the sarcomere length. To correct for these factors and make the results from different fibre bundles comparable, the intensities of the reflections were scaled by the intensity of the equatorial 1,0 reflection ($I_{1,0}$) at rest at the same SL as measured on the same pattern. The validity of this normalisation procedure depends on the finding that $I_{1,0}$ at rest in different fibres depends solely on the number of myofilaments in the X-ray beam as demonstrated by $I_{1,0}$ remaining intrinsically constant once corrected for the fibre mass under the beam (Reconditi et al 2014).

Data, from a total of eight bundles (4 controls and 4 PNB), are expressed as mean ± SEM.

Chapter 3. Results

3.1 PNB suppresses thick filament activation and motor attachment during tetanic stimulation and imposed stretch

Addition of 20 µM PNB to Ringer solution induces the complete suppression of force generation under tetanic stimulation (Fig. 3.1, A).

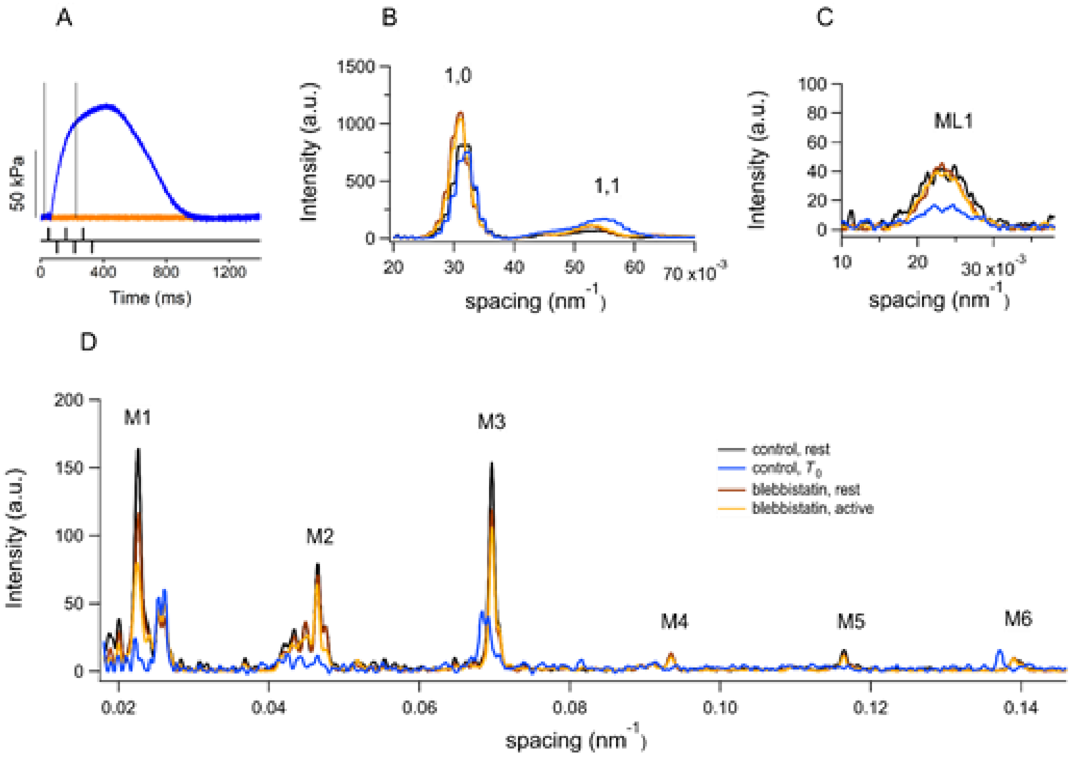

Figure 3.1. Effect of PNB on force and low-angle X-ray signals. A. Upper panel: force development during tetanic stimulation at 2.7 µm SL in normal Ringer (blue) and in the presence of 20 µM PNB (orange); gray bars: X-ray exposure windows. Lower panel: stimulus. **B-D**. Intensity profiles at rest (black, control; brown, in the presence of PNB) and during tetanic stimulation (blue, control; orange, PNB) of equatorial 1,0 and 1,1 reflections (B), first myosin layer line, ML1, (C) and myosin meridional reflections, M1-M6, (D).

The inhibitory effect progresses with the time from the start of perfusion of PNB, taking 30-40 min to be completed.

The structural correlate of the action of PNB at the level of the thick filament and myosin motors was tested by collecting 2D X-ray diffraction patterns at the ID02 beamline of the European Synchrotron Radiation Facility (ESRF, Grenoble, France). For the purpose of this work, the X-ray patterns were collected at SL 2.7 μm. This is, in fact, the largest SL at which X-ray data can be collected with minimal X-ray radiation damage (Reconditi *et al.*, 2014), and, from the other side, large enough to prevent lengthening response elicited by a force step to exceed the range of the motor movement (see Methods). The effect of PNB on the X-ray signals marking the structural state of the thick filament was determined by comparing low-angle X-ray patterns, collected at rest in normal Ringer solution, with those collected in the presence of PNB both at rest and during tetanic stimulation.

Fig. 3.1, B-D shows the superimposed intensity profiles of the relevant reflections in the 2D pattern: the equatorial reflections (1,0) and (1,1) (B), associated with the hexagonal lattice of thick and thin filaments, the first myosin-based layer line reflection (ML1) (C), associated with the three stranded helical periodicity of the myosin motors in the thick filaments (Huxley & Brown, 1967) and the meridional reflections (M1 to M6) (D), associated with the periodicity of myosin molecules along the axis of the thick filaments. In normal Ringer solution at rest (control condition, black lines in Fig. 3.1, B-D) the intensity of the (1,0) reflection ($I_{1,0}$) contributed from the lattice planes containing thick filaments, is relatively strong, while the intensity of the (1,1) reflection ($I_{1,1}$) contributed from the lattice planes containing both thin and thick filaments is less intense (Fig. 3.1, B black). At T_0 (blue), $I_{1,0}$ slightly reduces and $I_{1,1}$ increases so that their intensity ratio ($I_{1,1}/I_{1,0}$) increases from 0.13 ± 0.02 (Fig 3.2, A, black) to 0.66 ± 0.14 (blue) indicating that myosin motors have left the surface of the thick filament and moved toward the thin filament. The first myosin layer line (ML1), with an axial spacing ca 43 nm, is strong at rest (Fig. 3.1, C, black), marking the OFF state of myosin motors lying in helical tracks on the surface of the thick filament. The intensity of ML1 (I_{ML1}) weakens at T_0 (Figs. 3.1, C and 3.2, B blue), when the motors have left the surface of the thick filament and are either disordered or attached to actin. The meridional reflections M1-M6 indexing on an axial periodicity of ~ 43 nm are conventionally called “myosin-based” reflections, though other thick filament components are likely to contribute to the reflections, and MyBP-C in particular makes a significant contribution to the M1 reflection (Rome *et al.*, 1973; Huxley *et al.*, 2009; Luther *et al.*, 2011; Caremani *et al.*, 2021).

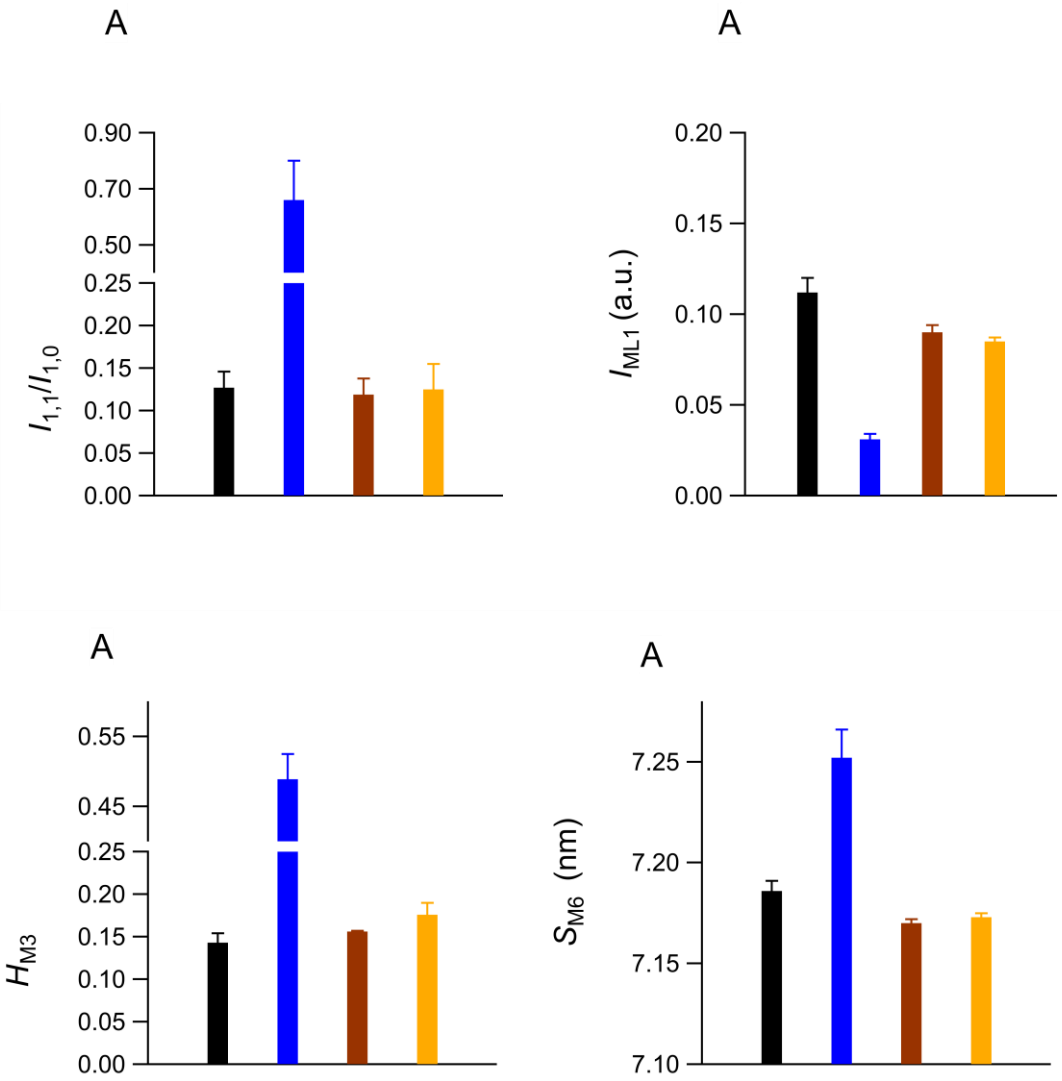

Figure 3.2. **Effects of stimulation on myosin motor and thick filament structure in normal Ringer and in the presence of PNB**. Same colour code as in Fig. 3.1. Ratio of the intensity of 1,1 reflection ($I_{1,1}$) over the intensity of 1,0 reflection ($I_{1,0}$); B. Intensity of ML1 reflection; C. Ratio of the high angle peak intensity of the M3 reflection over the total M3 intensity; D. Spacing of the M6 reflection. Error bars are SEM. Data from 6 fibres (n= 4-9.)

The intensity profiles of the meridional reflections in control conditions at rest (Fig. 3.1, D, black lines) undergo differential effects during development of T_0 (blue). The M3, associated with the myosin heads, and the M6, mainly contributed by the thick filament backbone, remain strong, while the M1 reflection, associated with MyBP-C, and the M2, M4 and M5, the so called “forbidden” reflections, associated with the perturbation of the axial repeat every three consecutive crowns within each 43-nm repeat, become very weak. M3 and M6 reflections, that remain strong during contraction, signal structural changes occurring upon stimulation in the myosin motors and the thick filament backbone, respectively. The M3 reflection exhibits a fine structure which arises from X-ray interference between the two arrays of myosin motors in each thick filament (Linari *et al.*, 2000) and represents a powerful tool for measuring, with subnanometer precision, the movements of myosin motors (Reconditi *et al.*, 2004). M3 at rest has a main peak corresponding to an axial periodicity of 14.34 nm and small satellite peaks on either side, with the one on the high angle side larger than that on the low angle side (Fig. 3.1, D, black). The ratio of the high angle peak intensity over M3 intensity (H_{M3}) is 0.14 ± 0.01 (Fig. 3.2, C, black). At T_0 the M3 reflection moves to a lower reciprocal spacing, corresponding to a roughly 1.3% increase in the axial periodicity along the thick filament and its fine structure changes to two main peaks of comparable intensity (H_{M3}= 0.49 ± 0.04; Figs. 3.1, D and 3.2, C, blue). Structural modelling based on the electron density maps of myofilaments in the relaxed state (Woodhead *et al.*, 2005) demonstrated that H_{M3} at rest is consistent with myosin motors lying on the surface of the thick filament tilted back in the OFF or IHM state (Reconditi *et al.*, 2011), while H_{M3} at T_0 is consistent with actin attached motors tilted beyond the perpendicular to the filament axis, 7 nm away from the resting motor orientation (Dobbie *et al.*, 1998; Piazzesi *et al.*, 2002; Piazzesi *et al.*, 2007; Reconditi *et al.*, 2011). The M6 reflection, mainly originated from a periodic mass distribution in the thick-filament backbone, is relatively insensitive to the conformation of the myosin motors and at rest has a periodicity (S_{M6}) of 7.186 ± 0.005 nm (Figs. 3.1, D and 3.2,D, black) that increases by about 1 % during contraction (blue), similar to the change in the spacing of the M3 reflection. These increases in spacing are 5 times larger than those expected on the basis of the elastic extensibility of the filament (Reconditi *et al.*, 2004; Reconditi *et al.*, 2019) and are correlated with slower stress-induced structural changes in the thick filament (Linari *et al.*, 2015). The perfusion of PNB Ringer solution does not affect the intensity profile at rest of either ML1 (Fig. 3.1, C, brown) or the meridional reflections (Fig. 3.1, D, brown). I_{ML1} (Fig. 3.2, B), H_{M3} (Fig. 3.2, C) and S_{M6} (Fig. 3.2, D) at rest are insensitive to PNB (compare black and brown, *t* test for the difference gives always $P>0.10$ with the exception of S_{M6} for which $P=0.05$).

Data in Fig. 3.2 are means from patterns in control and in the presence of PNB obtained from different fibres and the precise comparison of the intensities can be done only after removing the effect of the difference in cross sectional area, and thus in the number of myofilaments in the X-ray beam. For this each pattern has been divided by the intensity of the (1,0) equatorial reflection in the resting fibre at the same SL. The rationale of this normalisation procedure depends on the observation that $I_{1,0}$ at rest in the different fibres used for the comparison depends solely on the number of myofilaments in the X-ray beam (Reconditi *et al.*, 2014). The validity of the normalisation procedure in the present experiments relies on the evidence that PNB treatment at rest does not affect either H_{M3} (compare black and brown in Fig. 3.2, C, P= 0.31) and thus the OFF disposition of myosin motors along the thick filament, or the ratio ($I_{1,1}/I_{1,0}$) (compare black and brown in Fig 3.2, A) that depends on the fraction of motors on the surface of the thick filament. In PNB Ringer solution, upon tetanic stimulation all the parameters maintain the values characteristic of the resting state (Figs. 3.1 and 3.2 orange lines and orange columns) also at the time when in control the force attains the T_0 value (Fig. 3.1, A, blue line). Thus, PNB preserves the OFF state of the thick filament also during the rise of internal [Ca^{2+}] to the concentration that in control is responsible for the development of T_0.

The possible contribution of myosin motors to the lengthening response elicited by a force step imposed during tetanic stimulation in the presence of PNB was tested by comparing the X-ray signals in response to a step of ~0.25 $T_{0,c}$ (the isometric tetanic force developed in the control solution, at 4 °C and 2.15 μm SL) either at rest in control or during tetanic stimulation in the presence of PNB (Fig. 3.3, A). The lengthening transient elicited by the force step is much larger and slower at rest (blue) than during stimulation in PNB (orange) and the timing of the X ray window after the step is adjusted accordingly . As shown in Fig. 3.3, B-E, either at rest in control (black before step, blue after step) or during stimulation in PNB (brown before step, orange after step) no significant changes in the X-ray parameters marking the OFF state of the myosin motors accompany the response to the force step, except a ~0.4 % increase of the S_{M6} induced by the 0.25 $T_{0,c}$ force step both at rest (Fig. 3.3, E, blue versus black) or during tetanic stimulation (orange versus brown). The increase in S_{M6} underpins a thick filament extensibility of ~1.4%/T_0 (5 times larger than the filament compliance), which accompanies the stress-induced structural transition occurring in the thick filament in the time scale >1 ms (Reconditi *et al.*, 2004; Ma *et al.*, 2018; Reconditi *et al.*, 2019). The large, though not significant, reduction of I_{ML1} accompanying the response to the force step at rest (Fig. 3.3, C, blue versus black, -23%, P= 0.084) can be explained with the drop in I_{ML1} observed when a muscle at rest is brought to SLs higher than 2.7 μm (see Fig. 6A in (Reconditi *et al.*, 2014)). In fact, at rest (blue trace in Fig. 3.3, A), the lengthening induced by the 0.25 $T_{0,c}$ step (black) attains several tens of nm per hs. No I_{ML1} reduction occurs when the step is imposed in the presence of PNB (Fig. 3.3, C, orange versus brown), as it elicits a much smaller lengthening (Fig. 3.3, A, orange).

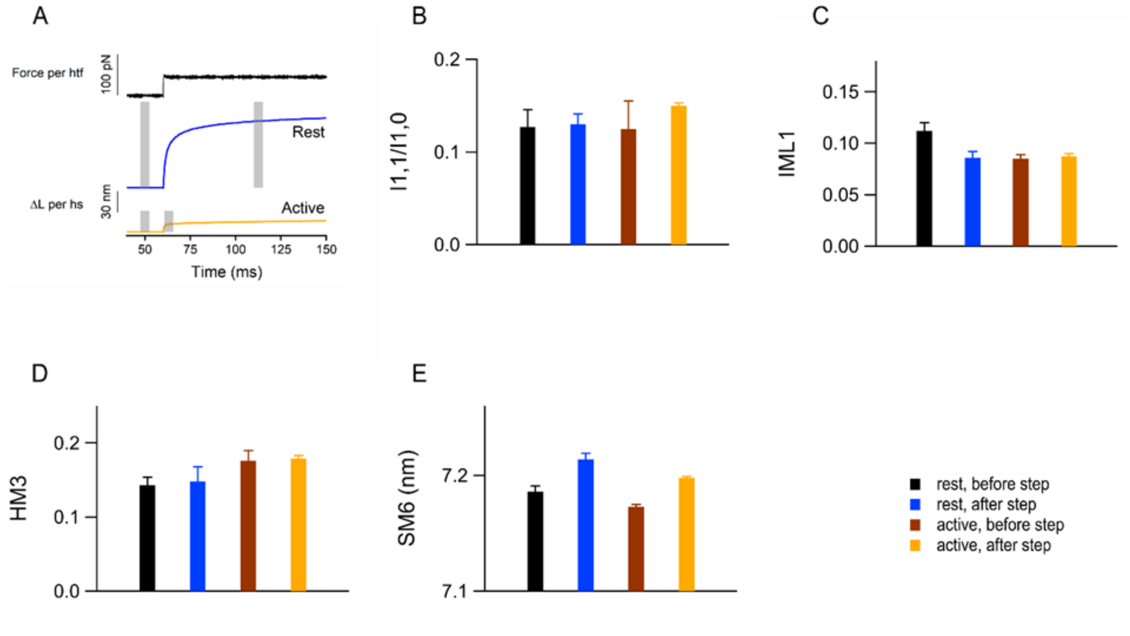

Figure 3.3. **Mechanical and X-ray diffraction responses to a force step**. A. half-sarcomere lengthening (coloured traces) to a force step of 0.25 T_0 imposed either at rest in normal Ringer solution (blue) or during tetanic stimulation in PNB Ringer solution (orange). Grey bars indicate the X-ray time windows. B-E. X-ray signals ($I_{1,1}/I_{1,0}$, B; I_{ML1}, C; H_{M3}, D; S_{M6}, E) collected before the step (black, rest; brown, during stimulation) and after the step (blue, rest; orange, during stimulation). Error bars are SEM. Data from 6 fibres (n= 4-9.)

In conclusion the X-ray analysis gives evidence that in the fibre activated in PNB as in the fibre at rest, the lengthening elicited by a force step does not produce any alteration of the OFF state of myosin motors.

3.2 During tetanic stimulation the I-band titin extensibility reduces by one order of magnitude and becomes independent of SL

PNB treatment allows the investigation of the effect of tetanic stimulation and of the underlying Ca^{2+} activation on the response of the half-sarcomere to a force step in the absence of the otherwise dominant effect of myosin motors.

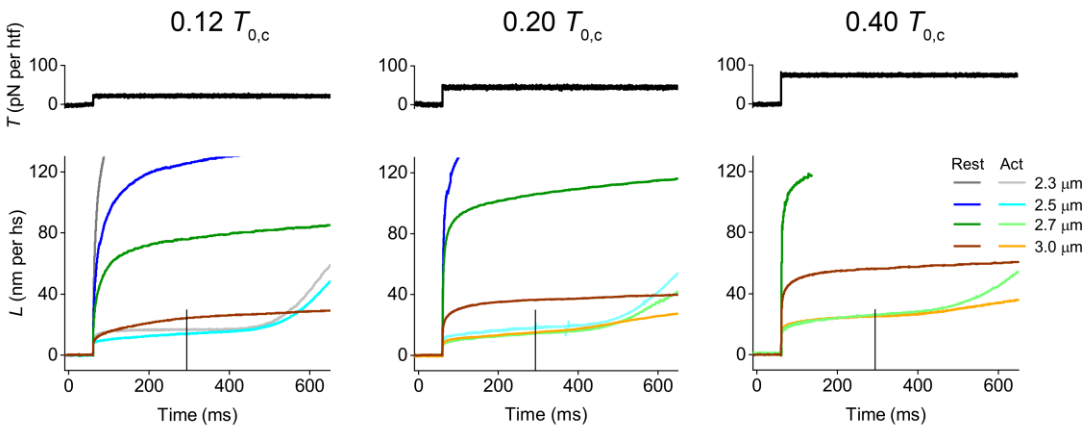

Fig. 3.4. **Dependence of lengthening on step size and sarcomere length**. Upper row: force steps of 0.12 $T_{0,c}$ (left column), 0.2 $T_{0,c}$ (middle column) and 0.4 $T_{0,c}$ (right column). Lower row: corresponding lengthening responses at rest (dark colours) and during stimulation (light colours) at four different sarcomere lengths (dark and light grey, 2.3 μm; blue and cyan, 2.5 μm; dark and light green, 2.7 μm; brown and orange, 3 μm). The vertical grey lines indicate the end of stimulation.

The lengthening responses of ~500 sarcomeres selected near the force transducer end of the fibre to force steps of amplitude ΔT= 0.12 $T_{0,c}$ (left column), 0.2 $T_{0,c}$ (middle column) and 0.4 $T_{0,c}$ (right column) at different sarcomere lengths (range 2.3 – 3.0 μm) are shown in Fig. 3.4. At rest (dark colours), even for the smallest step (0.12 $T_{0,c}$, left column), the lengthening response at 2.3 μm SL (dark grey) saturates the range of movement allowed by the motor (± 600 μm, see Methods). Thus, at rest the response of the fibre to a 0.12 $T_{0,c}$ step could be recorded at SL= 2.5 μm (blue) and above, showing that it is made by a fast, roughly exponential component complete within ~50 ms followed by a slow component at constant velocity (~15 nm s^{-1} per hs). The amplitude of the fast component progressively decreases at larger SL, being ~120 nm per hs at 2.5 μm SL (blue), ~60 nm per hs at 2.7 μm (green) and ~15 nm per hs at 3.0 μm (brown). A quantitative estimate of the amplitude of the fast component (L_2) is obtained as the ordinate intercept of the tangent to the later linear phase back-extrapolated to the time of the step (see Methods, Fig. 2.5). With force steps to 0.2 $T_{0,c}$ (middle column), also at 2.5 μm SL (blue) the lengthening response saturates the range of movement of the motor and L_2 could be determined only at 2.7 (green) and 3.0 μm (brown) SL. Equally, with a force step of 0.4 $T_{0,c}$ (right column) the lengthening response at 2.7 μm SL is just beyond saturation of the motor movement and L_2 could be determined only at 3.0 μm SL (brown). Thus, the hs at rest is quite extensible and becomes progressively stiffer with the increase in SL. Consequently, the range of movement of the motor system is adequate to measure L_2 in response to a 0.2 $T_{0,c}$ step only at SL ≥ 2.7 μm. As shown in Table 3.1, A (data from six fibres), L_2 for 0.2 $T_{0,c}$ is reduced to ½ (from 88 to 46 nm per hs) with the increase in SL from 2.7 to 3.0 μm. In these experiments $T_{0,c}$ is 142 ± 8 kPa, which, from the lattice geometry, corresponds to 241 ± 14 pN per half thick filament (htf), thus 0.2 $T_{0,c}$ corresponds to ~50 pN per htf. For simplicity let's define as a stiffness e_2 (= $\Delta T/L_2$) the quasi-static resistance to the increase in load that can be estimated from these responses. e_2 is ~0.6 pN/nm per htf at 2.7 μm SL and is almost double, ~1.1 pN/nm per htf, at 3.0 μm SL (Table 3.1, A).

SL (μm)	ΔT (pN per htf)	L_2 (nm per hs)	e_2 (pN/nm per htf)	t_{sw} (ms)	n
A					
2.7	50 ± 4	88.10 ± 4.32	0.61 ± 0.07		4
3.0	50 ± 5	46.10 ± 4.98	1.16 ± 0.13		9
B					
2.5	49 ± 3	15.93 ± 1.54	3.16 ± 0.19	166 ± 16	9
2.7	53 ± 3	16.82 ± 0.67	3.18 ± 0.16	212 ± 20	13
3.0	54 ± 3	14.53 ± 0.90	3.86 ± 0.25	169 ± 16	13

Table 3.1. Mechanical parameters of the lengthening response. The size of the fast lengthening (L_2), the stiffness (e_2) and switch time to steeper lengthening (t_{sw}) are estimated at rest (A) and during stimulation (B) following a force step (ΔT) of ~0.2 $T_{0,c}$ at three SL. Data from 6 fibres (A) and 8 fibres (B), n is the number of measurements contributing to the average. Errors are SEM. Temperature 4 °C.

The response to the force step during tetanic stimulation (active condition, light colours in Fig. 3.4) shows a dramatic increase in e_2. The fast component of the lengthening response (L_2) at the same SL is much smaller and briefer (half time within 500 μs) than that at rest, so that the response to the 0.2 $T_{0,c}$ step (middle column) could be recorded also at 2.5 μm SL. The later, almost linear slow lengthening occurs at a similar speed (~10 nm s^{-1} per hs) as at rest until, following the end of stimulation (vertical bar at 290 ms), it undergoes a sharp transition to a steeper lengthening. The time elapsed from the end of stimulation to this transition (t_{sw}, see Methods) is a clear indication of the delay with which the response of the sarcomeres at rest is resumed. Most strikingly, L_2 for a given force step in the active fibre is almost independent of SL: L_2 for 0.2 $T_{0,c}$ step (middle column) is ~10 nm per hs at the three SL's (2.5 μm, cyan; 2.7 μm light green and 3 μm, orange). Increasing the force step to 0.4 $T_{0,c}$ (right column), the lengthening response at rest saturates also at 2.7 μm SL (dark green) and can be recorded only at 3 μm SL (brown, ~50 nm per hs). In the active fibre, L_2 becomes much smaller and again almost independent of SL: L_2 is ~20 nm per hs at both 2.7 μm (light green) and 3 μm (orange) SL.

The lengthening responses of the active fibre to a 0.2 $T_{0,c}$ step (corresponding to ~50 pN per htf) at the three SL's (2.5, 2.7 and 3 μm) are summarized in Table 3.1, B (8 fibres): (*i*) the amplitude of L_2, is almost the same at the 3 SL's: ~16 nm at 2.5 and 2.7 μm SL and slightly smaller at 3.0 μm SL; (*ii*) the corresponding e_2, is ~3.2 pN/nm per htf at 2.5 and 2.7 μm SL and ~3.9 pN/nm per htf at 3.0 μm SL (the difference is not significant, P> 0.11); t_{sw}, the time after the end of stimulation at which the speed of lengthening switches to a higher value ranges from 160 to 210 ms and does not show any dependence on SL (P for the differences is always > 0.21). Notably the lengthening speed acquired after t_{sw} is higher at shorter SL, as shown by the final slope of the superimposed traces in the middle column of Fig. 3.4 (orange: 3.0 μm, light green: 2.7 μm and cyan: 2.5 μm). This is expected since after t_{sw} the extensibility of the resting fibre is resumed and thus the lengthening speed is related to the value of the resting L_2 that is larger at shorter SL.

The effect of the step size on the lengthening response at a given SL could be investigated at rest only at 3 μm SL, thus the comparative analysis of this phenomenon in resting and active fibres was conducted at 3 μm SL (Table 3.2). At this SL, e_2 is three times smaller at rest (1 - 1.5 pN/nm per htf) than during activation (3.1 - 3.9 pN/nm per htf). In both cases the larger step elicits a larger L_2, so that e_2 is not significantly affected by the force step amplitude, in fact even if at rest L_2 appears to increase with the step size less than in proportion to the step, the deviation from the direct proportionality is not enough to underpin a significant increase of e_2 with the step size (P always > 0.09).

In conclusion, the dependence of e_2 on SL (Table 3.1, A and B) shows that the extensibility of the hs at rest, which under the experimental conditions represents the extensibility of the I-band titin, reduces under tetanic stimulation by a factor that varies with SL: the factor is 3 at 3 µm SL and 6 at 2.7 µm SL. Moreover, inspections of the responses at shorter SL (Fig. 3.4) indicates that at 2.5 µm SL the I-band extensibility upon stimulation is reduced by a factor of 10 (compare the blue and cyan traces in the left column) and at 2.3 µm SL, at which the saturation of movement of the motor prevents from a quantitative evaluation, by a larger factor, likely more than 20 (compare dark and light gray traces). The phenomenon can be simply explained by considering that at rest the large extensibility of the I-band titin at short SL is accounted for by straightening of randomly bent elements of the proximal Ig domain portion (Linke *et al.*, 1998b).

ΔT (pN per htf)	L_2 (nm per hs)	e_2 (pN/nm per htf)	t_{sw} (ms)	n
A				
96 ± 15	63.59 ± 6.23	1.50 ± 0.09		3
50 ± 5	46.10 ± 4.98	1.16 ± 0.13		9
30 ± 2	31.43 ± 5.06	1.01 ± 0.15		4
B				
96 ± 13	31.56 ± 4.08	3.07 ± 0.27	171 ± 29	4
54 ± 3	14.53 ± 0.90	3.86 ± 0.25	169 ± 16	13
36 ± 2	12.92 ± 2.94	3.28 ± 0.76	208 ± 15	4

Table 3.2. Effect of step size on mechanical parameters. Three steps of different size are imposed at 3 µm SL at rest (A) and during stimulation (B). L_2, amplitude of fast lengthening; e_2, stiffness per htf; t_{sw}, switch time to steeper lengthening. Data from 8 fibres, n is the number of measurements contributing to the average. Errors are SEM. Temperature 4 °C.

The shorter the SL, the larger the extension required to get to the point at which the proximal Ig domain portion is straightened. On the other hand, if at 3.0 µm SL the Ig domain portion of the frog titin, as shown for the titin of the rabbit psoas myofibril

(Linke *et al.*, 1998a; Linke *et al.*, 1998b), attains its contour length, the lengthening in response to a force step is sustained only by the other serially linked spring, the PEVK region. Under these conditions the I-band extensibility is reduced to a minimum and e_2 attains the maximum value of 1-1.5 pN/nm per htf (Table 3.1). Upon tetanic stimulation e_2 becomes three times larger (3.1-3.9 pN/nm per htf, Table 3.1) than the maximum resting value and, more strikingly, does not vary with SL in the range of SL (2.5-3 μm) at which adequate statistics for the comparative analysis could be obtained. Actually, direct inspection of the responses of the active fibre in the left column of Fig. 3.4 provides the qualitative evaluation that the I-band extensibility at 2.3 μm SL (light grey) may be slightly larger than at longer SL (cyan).

We conclude that upon stimulation the I-band stiffness switches from the OFF state characterised by a large SL-dependent extensibility to an ON state characterised by a high, SL independent stiffness (≥3 pN/nm). The underlying mechanism must rely on a Ca^{2+}-dependent process that excludes the contribution of the compliant proximal Ig-domain region. The molecular basis of this mechanism and its kinetics have been investigated by determining how temperature affects the extensibility of the I-band titin at rest and during tetanic stimulation and extending the stiffness analysis to the high frequency domain to track the time course of the Ca^{2+}-dependent process and its temperature sensitivity.

3.3 Temperature does not affect the OFF and ON states of titin but controls the transition kinetics measured with 4kHz oscillations

The lengthening responses to a force step of 0.2 $T_{0,c}$ imposed at rest and during tetanic stimulation have been determined at 14 °C for the same SL's (2.5, 2.7 and 3.0 μm) as at 4 °C. From the simple superposition of the responses at 3 μm SL (Fig. 3.5), it is evident that in both resting 4 °C, blue and 14 °C, brown) and active conditions (4 °C, cyan and 14 °C, orange) the lengthening transient is quite similar at the two temperatures, indicating that the resting extensibility and the activation-induced threefold reduction in L_2 are not affected by temperature. The only evident effect of raising temperature is in t_{sw}, the time after the end of stimulation when the speed of lengthening switches from that characteristic of the active fibre to that of the resting fibre, becoming shorter. In this fibre, according to the optimisation of the stimulation parameters for the tetanus in control at 4 °C (frequency 20 Hz, 6 stimuli) and at 14 °C (60 Hz, 14 stimuli), the stimulation ends at 250 ms at 4 °C (cyan vertical line) and at 216 ms at 14°C (orange vertical line), and the corresponding t_{sw} are 183 and 56 ms at 4 and 14 °C respectively

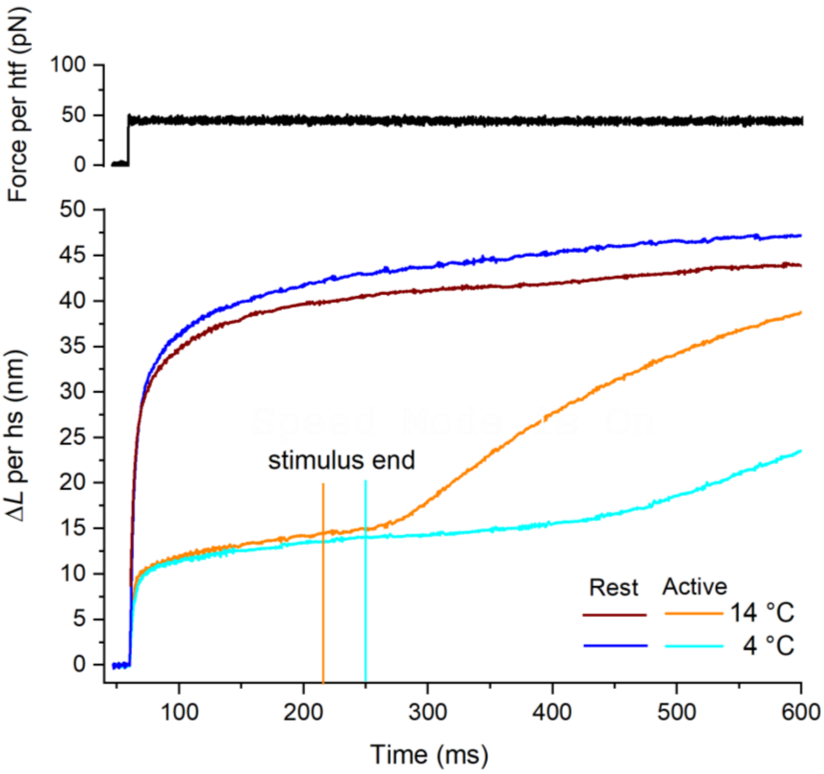

Figure 3.5. Effect of temperature on the lengthening responses (lower panel) to a force step of 0.2 T_0 (upper panel). Black, force; blue and cyan, 4°C; brown and orange, 14°C; dark colours, rest; light colours, active. SL, 3 µm. The vertical bars indicate the end of stimulation at the two temperatures according to the colour code.

The relevant parameters of the lengthening response at 14 °C in the SL range 2.7-3.0 µm (resting fibres) and 2.5-3.0 µm (active fibres) are summarised in Table 3.3. As at 4 °C, e_2 at rest increases with SL, while e_2 of the active fibre (3.3-3.9 pN/nm per htf) does not change significantly with SL (P always > 0.38). Moreover, at any SL both at rest and during activation e_2 is not significantly different from the corresponding value at 4 °C (P always >0.16). t_{sw} at 14 °C (50-70 ms) is threefold smaller than at 4 °C, but, as at 4 °C, does not change significantly with SL (P always > 0.45). Thus a 10 °C increase in temperature has no effect on the amplitude of the parameters that define the extensibility of the I-band spring in the resting and active fibre, but has a marked effect (Q_{10} ~3) on the kinetics of the transition from the response typical of the active fibre to that of the resting fibre, following the end of stimulation.

SL (µm)	ΔT (pN per htf)	L_2 (nm per hs)	e_2 (pN/nm per htf)	t_{sw} (ms)	n
A					
2.7	58 ± 5	79.07 ± 5.02	0.74 ± 0.07		5
3.0	52 ± 5	40.58 ± 8.44	1.52 ± 0.39		5
B					
2.5	48 ± 5	14.71 ± 1.30	3.29 ± 0.32	59 ± 5	3
2.7	52 ± 3	14.18 ± 0.71	3.88 ± 0.32	70 ± 9	6
3.0	50 ± 4	13.66 ± 0.94	3.80 ± 0.42	64 ± 5	8

Table 3.3. Mechanical parameters of the lengthening response at 14 °C. Size of the fast lengthening (L_2), stiffness per htf (e_2) and switch time to steeper lengthening (t_{sw}) at rest (A) and during stimulation (B) following a force step (ΔT) of ~0.2 T_0 at three SL. Data from 5 fibres, n is the number of measurements contributing to the average. Errors are SEM. Temperature 14 °C.

The lengthening transient, through the parameter t_{sw}, is able to record the transition kinetics from stiff (ON) to extensible (OFF) state of the I-band titin spring, but cannot *per se* have the time resolution to describe the OFF-ON transition at the start of stimulation. In fact, the fast phase of the lengthening transient takes a few tens of milliseconds to be completed, a time that might be comparable to that taken by the Ca^{2+}-dependent activation process triggered by the stimulation. Consequently, the lengthening transient elicited by a force step imposed at different times early after the start of stimulation would be inadequate to define the switching ON of titin stiffness, because the lengthening transient itself would be complicated by the merging of the two processes.

A method with the time resolution adequate to describe the Ca^{2+}-dependent transition in the I-band titin stiffness is the imposition of small (1.5 nm per hs peak to peak) 4 kHz oscillations throughout, from before the start of stimulation (taken as 0 time) to beyond the time after the end of stimulation when the resting extensibility is recovered (Fig. 3.6). Measurements had to be done at 3.0 µm SL, at which a minimum low passive force and stiffness allow the transmission of perturbation through the fibre from the motor end to the force transducer end. The inertial effect due to the acceleration of the fibre at the motor end reduces progressively throughout the fibre, making it possible to record an elastic response also under the low stiffness condition of the resting fibre, provided that the force signal (T) is related to the length oscillation measured on the sarcomere population near the force transducer end (L) (Fusi *et al.*, 2014a; Powers *et al.*, 2020).

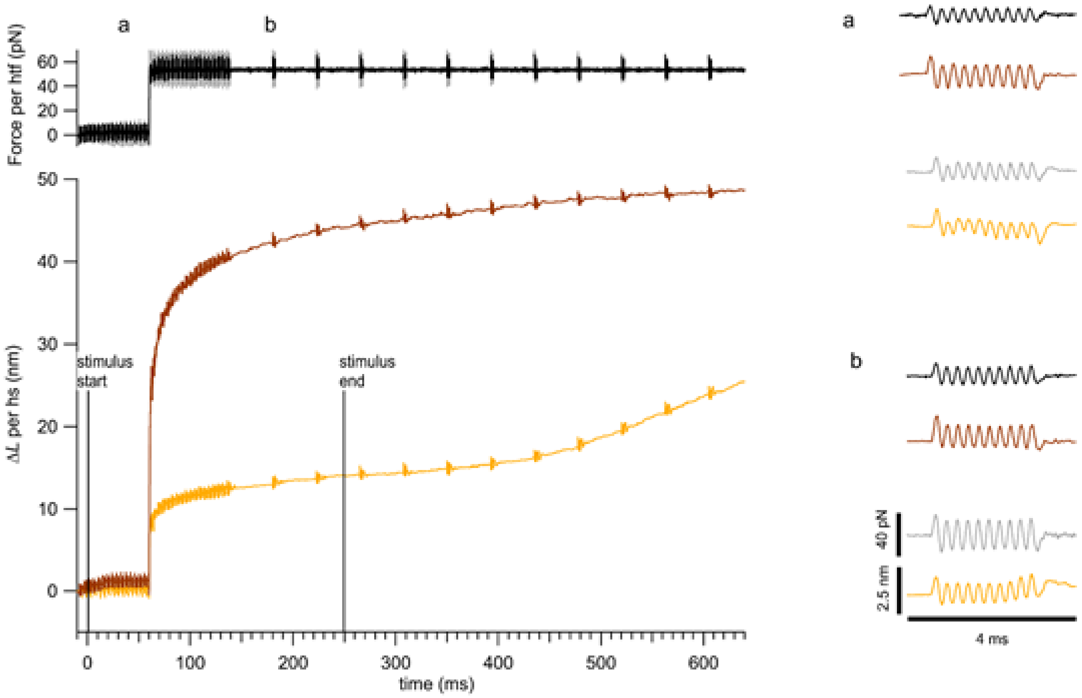

Figure 3.6. Force and length responses to 4 kHz oscillations superimposed to the response to a force step of 0.2 T_0. Left: upper panel, force; lower panel, length change. Black and brown, rest; grey and orange, active. The black vertical lines indicate stimulus start and stimulus end related to the active response. a and b indicate the times of the expanded traces on the right, drawn with the same colour code as on the left.

Under these conditions, the Fourier analysis of T versus L provides an elastic modulus that is a good estimate of the quasi-instantaneous stiffness (e_1). At 4 °C (Fig. 3.7, A, open symbols and Table 3.4, A) before stimulation e_1 is 9.5 pN/nm per htf (open circles) and is accompanied by a phase lead of T versus L (φ positive) of 19.4 ° (open triangles), as expected from the presence of a dominant viscoelastic element in the resting fibre responsible for the large rapid lengthening following the force step at any SL. The start of stimulation induces an increase in e_1 which attains a plateau value of 14.4 pN/nm per htf (+ 51 %) with an approximately sigmoidal time course (Fig. 3.7, A open circles and Table 3.4, A).

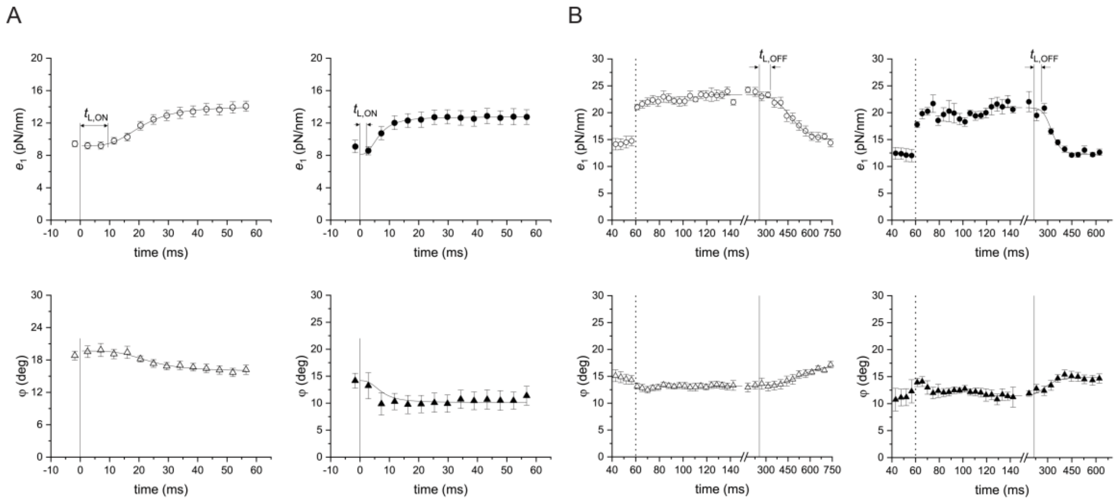

Figure 3.7. Time courses of elastic modulus and phase shift following stimulation and force step. A. Changes in elastic modulus (e_1, circles, upper row) and phase shift (φ, triangles, lower row) following the start of stimulation, marked by the vertical continuous line at zero time. Open symbols: 4 °C, filled symbols: 14 °C. Continuous lines are sigmoidal fits to data points to estimate the half-time of the changes following the start of stimulation ($t_{1/2,\mathrm{ON}}$) and the time to 5% of total change (latency time $t_{\mathrm{L,ON}}$). In all cases, except for filled triangles, all parameters are free. The fit to filled triangles is obtained by leaving as the only free parameter the end point of the sigmoid and taking the other parameters from the fitted open triangles scaled by the Q_{10} calculated from $t_{1/2,\mathrm{ON}}$ of the fit to circles. $t_{\mathrm{L,ON}}$ at 14 °C is calculated by applying the Q_{10} of $t_{1/2,\mathrm{ON}}$ to the value measured at 4 °C. **B.** Changes in elastic modulus (e_1, circles, upper row) and phase shift (φ, triangles, lower row) following a 0.2 T_0 force step imposed during stimulation at the time marked by the dashed line and followed by the end of stimulation, marked by the vertical continuous line. Open and filled symbols as in A. Continuous lines are sigmoidal fits to data points to estimate the half-time of the changes following the end of stimulation ($t_{1/2,\mathrm{OFF}}$) and the time to 5% of total change (latency time $t_{\mathrm{L,OFF}}$); all parameters are free. $t_{\mathrm{L,OFF}}$ at 14 °C is calculated by applying the Q_{10} of $t_{1/2,\mathrm{OFF}}$ to the value measured at 4 °C.

Meanwhile, φ decreases in a way specular to the increase in e_1, attaining 14.7 ° (-24 %) with a similar time course (Fig. 3.7, A open triangles and Table 3.4, A). To give the best quantitative estimate of the time course of the events induced by the stimulation, the time parameters are measured with a sigmoidal fit of the average e_1 points versus time after the start of stimulation (continuous lines in Fig. 3.7). There is a latency before e_1 starts to increase after the first stimulus ($t_{\mathrm{L,ON}}$), which is 9.4 ms as estimated by the time from the 1st stimulus to 5% of the total change estimated by the sigmoidal curve. The half-time ($t_{1/2,\mathrm{ON}}$) for e_1 to rise to the active plateau value is 21 ms (Table 3.5). Increase of temperature to 14 °C (Fig. 3.7, A, filled symbols and Table 3.4, B) slightly reduces both e_1 and φ both at rest (P = 0.039 and 0.002 respectively) and after stimulation (P = 0.039 and 0.015 respectively) (Table 3.4, B). The specular response to the stimulation of e_1 and φ is maintained (Fig. 3.7, A, filled circles and filled triangles respectively and

Table 3.4, B): e_1 rises from 8.55 to 12.2 pN/nm per htf (+43%) and φ reduces from 16.3 to 11.3° (-30 %), both changes being significant ($P < 0.001$). Otherwise, the increase in temperature to 14 °C speeds up by a factor of 3 the time courses of the events so that $t_{1/2,\mathrm{ON}}$ decreases to 6.5 ms (Fig. 3.7, A filled circles and Table 3.5). Also $t_{\mathrm{L,ON}}$ decreases, but the value cannot be reliably defined for the limits of the time resolution. A value of 2.9 ms (short bar in Fig 3.7, A, upper right panel and Table 3.5) has been estimated by applying the Q_{10} calculated from $t_{1/2,\mathrm{ON}}$ (3.22) to the $t_{\mathrm{L,ON}}$ value measured at 4 °C.

A			e_1 (pN/nm per htf)	φ (deg)	n
Before step	Rest		9.53 ± 0.20	19.38 ± 0.46	63
	Active		14.38 ± 0.49	14.68 ± 0.46	32
		step size (pN)			
After step	Rest	51 ± 7	13.93 ± 0.19	18.06 ± 0.21	75
	Active	59 ± 5	22.85 ± 0.18	13.15 ± 0.13	176
	Post stimulus		15.28 ± 0.38	16.36 ± 0.25	34

B			e_1 (pN/nm per htf)	φ (deg)	n
Before step	Rest		8.55 ± 0.27	16.31 ± 0.52	46
	Active		12.24 ± 0.52	11.34 ± 0.86	20
		step size (pN)			
After step	Rest	58 ± 7	12.16 ± 0.25	16.00 ± 0.25	57
	Active	59 ± 6	20.31 ± 0.28	12.11 ± 0.20	84
	Post stimulus		12.49 ± 0.24	14.71 ± 0.36	23

Table 3.4. Elastic modulus (e_1) and phase shift (φ) as measured with 4 kHz oscillations before and after the force step, both at rest and during stimulation. A. 4 °C, B. 14 °C. Data from four fibres. n indicates the number of repeats contributing to each average. Errors are SEM. Time intervals for average are: rest, before step, 55 ms; active, before step, 15 ms; rest and active after step, 125 ms; post stimulus, 150 ms and 190 ms at 4 °C and 14 °C respectively.

When a force step of 0.2 $T_{0,c}$ is imposed on the active fibre (vertical dashed lines in Fig. 3.7B), the rapid lengthening response (~15 nm per hs) is accompanied by a synchronous increase in e_1 that is similar at both temperatures (Fig. 3.7, B upper panels)): e_1 attains 22.85 pN/nm per htf (+59% with respect to the value before the step) at 4 °C (Table 3.4, A), and 20.31 pN/nm per htf (+66%) at 14 °C (Table 3.4, B). Thus, the increase in e_1 with the force step is relatively larger than that induced by activation and, most importantly, occurs while φ undergoes either a minor reduction (-10%, P = 0.01, 4 °C, Table 3.4, A), or no change (+6.8%, P = 0.47, 14°C, Table 3.4, B). When the force step of 0.2 $T_{0,c}$ is imposed on the resting fibre, the three times larger lengthening (~45 nm per hs) is accompanied by similar increases of e_1 both at 4 °C (from 9.5 to 13.9 pN/nm per htf , +46 %, P <0.0001, Table 3.4, A) and at 14°C (from 8.55 to 12.2 pN/nm per htf, +42 %, P<0.0001, Table 3.4, B), without a significant change in φ with respect to the basic resting value at the same temperature (Table 3.4, A and B).

Temperature (°C)	$t_{1/2,\mathrm{ON}}$ (ms)	$t_{\mathrm{L,ON}}$ (ms)	$t_{1/2,\mathrm{OFF}}$ (ms)	$t_{\mathrm{L,OFF}}$ (ms)
4	20.9 ± 0.6	9.35	220 ± 22	62
14	6.5 ± 0.5	2.9*	109 ± 6	31*

Table 3.5. Times for switching ON and OFF of the changes of elastic modulus e_1 at the start and at the end of stimulation. $t_{1/2,\mathrm{ON}}$ and $t_{1/2,\mathrm{OFF}}$, times to 50% of the total change of e_1 from the first and last stimulus, respectively, estimated with the sigmoidal fits (in Fig. 3.7 A and B, respectively). $t_{\mathrm{L,ON}}$ and $t_{\mathrm{L,OFF}}$, times to 5% of the total change estimated with the sigmoidal fits. The stars indicate that at 14 °C, given the paucity of data points, the values of $t_{\mathrm{L,ON}}$ and $t_{\mathrm{L,OFF}}$ are calculated by applying the corresponding Q_{10} of $t_{1/2,\mathrm{ON}}$ and $t_{1/2,\mathrm{OFF}}$ to the values measured at 4 °C.

Following the end of stimulation e_1 decreases and φ increases by similar amounts independent of temperature (~-35% e ~+22% respectively, post-stimulus row in Table 3.4, A (4 °C) and 3.4, B (14 °C). The steady values attained by e_1 and φ approach the values characteristic of the resting state after the step. The changes accompanying the recovery of the resting state (OFF transition) are ten times slower than those shown by the activation dependent rise (ON transition). The half-time for the OFF transition ($t_{1/2,\mathrm{OFF}}$), measured from the time of the last stimulus (vertical continuous line in Fig. 3.7, B) to 50% of total change estimated by the sigmoidal fit to data, is 220 ms at 4 °C and 109 ms at 14 °C (Table 3.5), showing a Q_{10} of 2.0. Also the latency of the OFF transition, $t_{\mathrm{L,OFF}}$, is one order of magnitude larger than that of the ON transition: at 4 °C

$t_{L,OFF}$, estimated by the time from the last stimulus to 5% of total change estimated by the sigmoidal fit (vertical bar), is 62 ms. At 14 °C $t_{L,OFF}$ decreases, with respect to the value at 4 °C, to a value that cannot be reliably defined for the paucity and the variability of points. The value of 31 ms (short bar in Fig 3.7, B, upper right panel and Table 3.5) is calculated by applying the Q_{10} of $t_{1/2,OFF}$ (2.0) to the $t_{L,OFF}$ value measured at 4 °C.

The results of the 4 kHz oscillation analysis reveal that the response to a force step imposed on the fibre, either active or resting, is characterised by increase in stiffness without significant change in phase, suggesting that the step induces a rise along the force-extension curve of the I-band titin spring that has nonlinear characteristics. Following the start of tetanic stimulation, the ensuing rise of $[Ca^{2+}]_i$ induces an increase in stiffness accompanied by a reduction in phase shift, indicating a change in the I-band titin spring from one less stiff and more viscoelastic to one much more stiff and less viscoelastic. This process is reversibly controlled by Ca^{2+} activation: at the end of stimulation the ensuing drop in $[Ca^{2+}]_i$ is accompanied by the recovery of the resting values of e_1 and φ. Noteworthy, the half-time of the recovery of these parameters, $t_{1/2,OFF}$, and its temperature dependence, uniquely defined at 3 µm SL, are comparable to the time and the temperature dependence of t_{sw}, the parameter that marks the OFF transition in terms of change in extensibility of the I-band titin spring at any SL (Tables 3.1-3.3).

3.4. The OFF-ON transition is explained by binding of a titin domain distal to the proximal poly-Ig domain to the nearest actin monomer.

The extensibility of the I-band titin spring in the fibre at rest is incommensurably large at full filament overlap and reduces progressively with the increase in SL, marking the OFF state of titin, in which the I-band titin elasticity is governed by the large extensibility of the proximal Ig domain portion until this portion attains its contour length, which putatively happens at a SL of ~3 µm (Fig 1.3). At this SL the I-band width, and thus the I-band titin end-to-end distance is 700 nm. The high resistance to stretch of the I-band titin spring found in the active fibre also at physiological SL (2.3-

2-5 μm) and its independence of SL (and thus of the I-band width) sign the ON state of titin (Fig. 3.4 and Table 3.1). The OFF to ON transition of the I-band titin spring triggered by fibre activation can be recorded with adequate time resolution with small 4 kHz oscillations imposed at 3 μm SL (Fig. 3.7 and Table 3.4). At this SL the proximal Ig domain region approaches the contour length and the stiffness of the passive fibre is lower but comparable to that of the active fibre. Under these conditions the OFF - ON transition is marked by a change in the spring from more to less viscoelastic. The time courses of the transition of the I-band titin from OFF to ON at the start of stimulation (Fig. 3.7, A and Table 3.5) and of the return to the OFF state after the end of stimulation (Fig. 3.4, Fig 3.7, B, Table 3.1 and Table 3.5) are temperature sensitive, but the mechanical features marking the OFF and the ON states are the same independent of temperature (Fig. 3.5 and Tables 3.1-3.4).

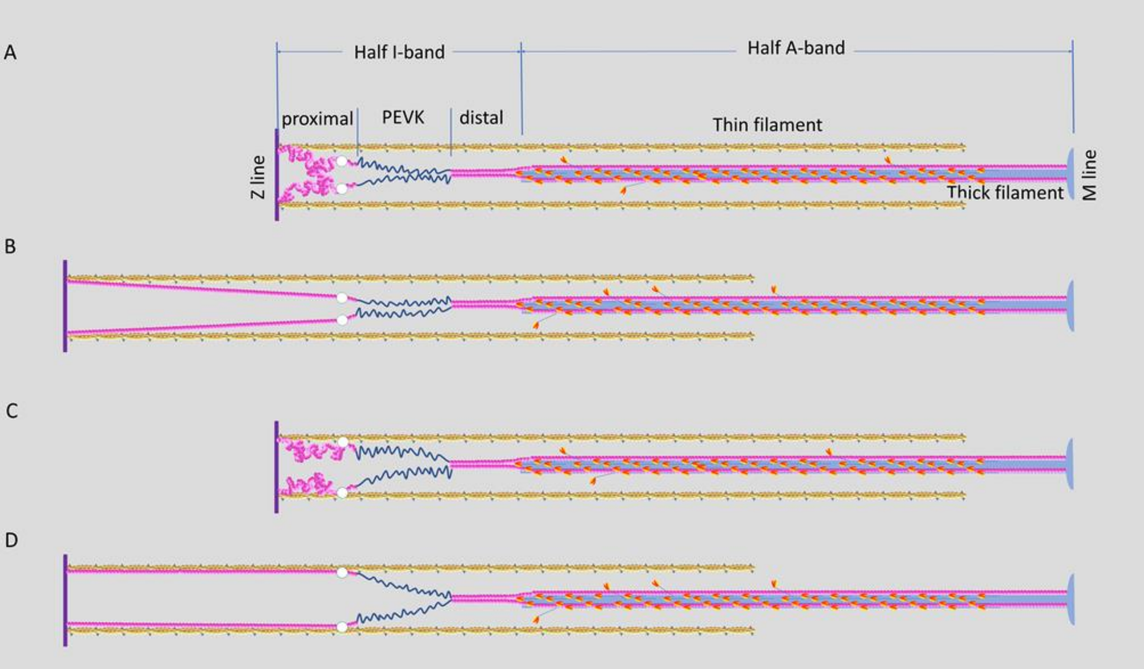

Fig. 3.8. Schematic of the OFF and ON states of titin at two different SL. A and **B**, OFF state at 2.3 and 3 μm SL respectively. In the sarcomere at rest I-band titin end-to-end distance corresponds to I-band width. The colour code for the various proteins of the sarcomere is the same as in Fig. 1.3 with the exception of the white circles distal to the proximal Ig domain representing the N2A domain on the titin molecule able to bind actin upon activation. **C** and **D**, ON state at the same SLs as A and B in the active fibre. Upon stimulation N2A domain identified with the white circle binds to actin reducing the length of the I-band titin spring independently of SL, to that of the distal portion in which the spring is mainly represented by the PEVK region.

The explanation of the titin response to activation must rely on a mechanism that, with titin in the ON state, is able to select a unique I-band titin spring, independent of SL, with a resistance to stretch that is higher but comparable to that of the titin in the

OFF state at 3 μm SL. The only explanation is that, with the rise of internal Ca^{2+}, a region in the I-band titin, distal to the proximal Ig domain region (white disk in Fig. 3.8, C), binds to actin and excludes the proximal Ig domain from contributing to the mechanical response, by substituting it with the much stiffer actin filament. Under these conditions the mechanical properties of I-band titin in the ON state depend on the titin portion (mainly the PEVK region) distal to the point of attachment to actin, independent of the SL at which the OFF-ON transition occurs (Fig. 3.8, C and D). In this way I-band titin becomes a tunable spring that in the muscle at rest (I-band titin in the OFF state) can accommodate different SL's exploiting the extensibility of the proximal Ig domain region (Fig. 3.8, A-B), while during muscle contraction (I-band titin in the ON state) it opposes to I-band extension with a stiffness, ~3 pN/nm per htf, that is the same at whatever SL. The underlying mechanism implies that the rise in internal [Ca^{2+}] not only triggers the myofilament activation, but also switches titin ON by promoting the binding of the titin point between the PEVK region and the proximal Ig domain region to the nearest point along the actin filament that is selected according to the SL (Fig. 3.8, C-D).

A molecular evidence in support of this mechanism comes from recent in vitro experiment (Dutta *et al.*, 2018) on the affinity for the actin filament of a construct of the N2A titin domain, which in the skeletal muscle links the proximal Ig domain region to the PEVK region (white disk in Fig. 3.8). It was found, with co-sedimentation measurements, that Ca^{2+} significantly increases the affinity of N2A for the actin filament and, with AFM force spectroscopy, that Ca^{2+} induces a 40% increase (from 70 to 100 pN) in the rupture force of the actin-N2A bond. In front of the dramatic effects of the Ca^{2+}-dependent OFF-ON switch of the I-band titin *in situ* found here, the *in vitro* measurements appear to underestimate the effect of Ca^{2+}. However, these *in vitro* measurements appear to underestimate the effect of Ca^{2+}. In fact, we find that, in the fibre at rest ([Ca^{2+}] <10^{-7} M), at 2.3 μm SL (dark grey trace in Fig. 3.4) the lengthening response to a force step as low as 0.12 $T_{0,c}$ or 30 pN per htf, that is (30/6 =) 5 pN per titin molecule, is so large to saturate the range of the loudspeaker-motor movement; moreover, this large extensibility is SL-dependent, reducing progressively with the increase in SL. These results are fully accounted for by attributing the response to the progressive straightening out of randomly bent elements in the proximal Ig-domain region and, moreover, demonstrate that at rest there cannot be any bond at a point distal to the proximal Ig-domain able to resist a force ≥5 pN. Under these conditions *in vitro* measurements showing a rupture force of the N2A-actin bond of 70 pN in Ca^{2+}-free solution appear to overestimate the strength of the N2A-actin bond in the absence of Ca^{2+} and thus underestimate the Ca^{2+} induced changes.

The apparent contradiction between *in vitro* and *in situ* results suggests that the access to the actin site for titin binding could be controlled by a Ca^{2+}-dependent structural transition in the thin filament that is lost in the *in vitro* experiment.

3.5. The kinetics of OFF-ON transition of the I-band titin is accounted for by Ca $^{2+}$-dependent thin filament activation

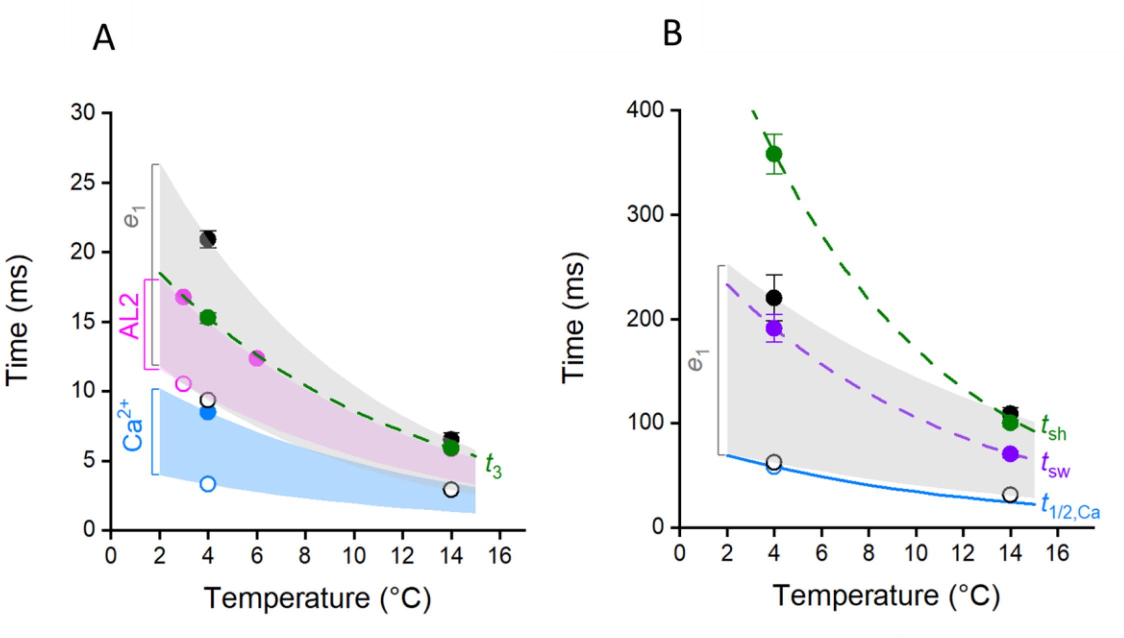

Fig. 3.9. Temperature dependence of ON and OFF transitions. A. ON transitions of the relevant parameters as defined in the text. Circles (values from Table 3.6) and shaded areas describe the transient defined by the colour in the range of temperatures of interest according to the analysis reported in the text. Blue open circle, Ca^{2+} transient start; blue filled circle, time to Ca^{2+} peak; blue shaded area temperature dependence of Ca^{2+} rise. Magenta open circle, start of AL2 increase; magenta filled circles, half-time of AL2 rise; magenta shaded area, temperature dependence of AL2 rise. Black open circles, $t_{L,ON}$; black filled circles, $t_{1/2,ON}$; grey shaded area, temperature dependence of e1 rise. Green circles and green dashed line, latency of force development t3 and its temperature dependence. **B**. OFF transitions of the relevant parameters as defined in the text. Blue open circle and blue line, $t_{1/2,Ca2+}$ and its temperature dependence; black open circles, $t_{L,OFF}$; black filled circles, $t_{1/2,OFF}$; grey shaded area, temperature dependence of e_1 drop; violet filled circles and dashed line: t_{sw} and its temperature dependence. Green filled circles and dashed line, t_{sh} and its temperature dependence.

The hypothesis that the OFF-ON switch in the I-band titin spring is induced by the rise of $[Ca^{2+}]_i$ finds support in a comparative analysis of time courses of the OFF-ON titin transition and of the Ca^{2+}-related signals accompanying contraction-relaxation of frog muscle fibre. The analysis concerns either directly the changes in $[Ca^{2+}]_i$ in response to action potentials or the ensuing structural and mechanical events in myofilaments. At 4 °C $[Ca^{2+}]_i$ starts to rise at 3.3 ms (blue open circle in Fig. 3.9, A and Table 3.6) after the foot of the action potential and attains its peak at 8.5 ms (blue filled circle and Table 3.6) (Caputo *et al.*, 1994; Sun *et al.*, 1996). These features of the Ca^{2+} transient can be defined for the range of temperatures in the present experiments (4-14°C, blue shaded area in Fig. 3.9, A) by taking into account a Q_{10} of 2.5 (Miledi *et al.*, 1982; Eusebi & Miledi, 1983).

ON transitions (ms)	Ca^{2+}		**°C**	**Q_{10}**
	$t_{L,Ca^{2+}}$	3.3	4	2.5
	$t_{p,Ca^{2+}}$	8.5	4	2.5
	AL2			
	$t_{L,AL2}$	10.5	3	
	$t_{1/2,AL2}$	16.74 ± 1.05	3	2.63
		12.32 ± 0.34	6	
		5.85 ± 0.62	14	
	e_1			
	$t_{L,ON}$	9.35	4	
		2.9*	14	
	$t_{1/2,ON}$	20.9 ± 0.6	4	3.22
		6.5 ± 0.5	14	
	Tetanus			
	t_3	15.26 ± 0.38	4	2.45
		5.87 ± 0.12	14	
OFF transitions (ms)	Ca^{2+}		**°C**	**Q_{10}**
	$t_{1/2,Ca^{2+}}$	58	4	2.4
	e_1			
	$t_{L,OFF}$	62	4	
		31*	14	
	$t_{1/2,OFF}$	220 ± 22	4	2.02
		109 ± 6	14	
	t_{sw}			
		191.2 ± 13.4	4	2.70
		70.56 ± 3.4	14	
	Tetanus			
	t_{sh}	358 ± 19	4	3.58
		100 ± 3	14	

Table 3.6 Relevant kinetic parameters accompanying transition to the ON-OFF state of the I-band titin.

The ensuing structural event in the thin filament, triggered by Ca^{2+} binding to Tn, is the azimuthal movement of Tm around the filament surface that makes the actin sites available for binding of the myosin motors (Gordon *et al.*, 2000). The movement of Tm in the thin filament during the activation of frog muscle contraction has been determined with time-resolved X-ray diffraction measurements of the changes in the intensity of the 2nd actin layer-line (AL2), sensitive to the position of Tm in the thin filament (Kress *et al.*, 1986): from Fig. 3 of Kress *et al.*, in which data collected at 3 °C have an adequate time resolution, it is possible to estimate that the azimuthal movement of Tm starts at 10.5 ms from the first action potential (magenta open circle, Table 3.6); the half-time for the completion of this process (measured by the time taken to reach 50% of the maximum change of the amplitude of the AL2 reflection) is 16.7 ms at 3 °C and reduces increasing the temperature as shown by magenta filled circles (estimated from Fig. 6a and b in Kress et al., 1986 and reported in Table 3.6).

The relative Q_{10} (2.63) can be used to calculate how the latency for the Tm movement reduces with temperature and draw the magenta shaded area that defines the time course of Tm movement (that is of the switching ON of the thin filament) for the range of temperatures of interest. How do these signals relate to the switching ON of the I-band titin elasticity can be defined by plotting the time following the first stimulus at which e_1 starts to increase ($t_{L,ON}$, Fig. 3.9, A, black open circles, from Tables 3.5 and 3.6) and the time at which e_1 attains the half -maximum value ($t_{1/2,ON}$, Fig. 3.9, A, black filled circles, from Tables 3.5 and 3.6). The grey shaded area, calculated by using the respective Q_{10}, defines the time course of the ON transition of the I-band titin. Considering the different source of the data plotted in Fig 3.9, A, it is impressive how strict and unique is the sequence of events that switches I-band titin elasticity ON: rise of $[Ca^{2+}]_i$ following the membrane depolarisation triggers the structural change in the thin filament regulatory complex leading to Tm movement around the thin filament that releases the actin sites for titin binding. Most importantly in terms of the molecular mechanism, Fig. 3.9, A not only defines a temporal sequence, but finds a solid explanation for the relatively long time taken by titin to switch ON (Fig. 3.7), in spite of the much faster rise in $[Ca^{2+}]_i$: I-band titin binds to actin at a rate that is limited by the time taken by Tm along the thin filament to move away, without any further significant delay. These results indicate that the classical role of Tm as the protein that regulates the possibility for myosin in the A-band to attach to actin and generate force must be integrated with a complementary role of Tm as the protein that regulates the possibility for a region of the I-band titin, distal to the proximal Ig-domain region, to attach to actin and become a stiff, SL-independent spring. This new regulatory role of the thin filament explains in turn the large difference in the effectiveness of the Ca^{2+} control of titin elasticity *in situ* (this paper) and *in vitro* (Dutta *et al.*, 2018).

Myosin attachment to actin and force generation are relatively slow with respect to the structural changes signalling thin filament activation (Kress *et al.*, 1986; Matsuo & Yagi, 2008; Tamura *et al.*, 2009; Fusi *et al.*, 2014b) and are subjected to another regulatory mechanism in the thick filament that switches ON the myosin motors in relation to the filament stress only in loaded contractions (Linari *et al.*, 2015; Piazzesi *et al.*, 2018). The time elapsed between the start of the action potential depolarization and the start of force rise in the isometric tetanic contraction at full overlap (t_3 according to the definition of (Mulieri, 1972; Haugen, 1982), insets of Fig 3.10, A,) is 14 ms at 4 °C (upper panel) and 5 ms at 14 °C (lower panel). t_3 has a minor dependence on SL: from 2.15 to 2.7 μm SL it increases by 16 % at 4 °C (Fig. 3.10, B upper panel) and by 21 % at 14 °C (lower panel). The average values of t_3 at either temperature (Fig. 3.9, A green circles and Table 3.6) and the relation calculated with their Q_{10} (2.45, green line) show that t_3 occurs at the time when the Tm movement along the thin filament is half-complete. t_3 coincides also with the time required to develop the maximum shortening velocity in unloaded conditions (V_0) (Lombardi & Menchetti, 1984; Brunello *et al.*, 2006). V_0 shortening is not expected to depend on the number of motors available for interaction with actin (Huxley, 1957) and indeed only 1-4 motors per hs are necessary ((Fusi *et al.*, 2017)), while most of myosin motors remain in their OFF state (Linari *et al.*, 2015). The temporal correspondence between actin filament activation, as measured by Tm movement, and attainment of V_0 shortening capability strengthens this view, showing that the rate limiting step for V_0 is the availability of actin sites on the thin filament.

A comparative analysis of the return of the various parameters to the resting state (OFF transitions) is attempted in Fig. 3.9, B. In a frog muscle fibre at 4 °C at full overlap the half-time for $[Ca^{2+}]_i$ decay after the last action potential of a short tetanus (duration 400 ms, Fig 4D in (Caputo *et al.*, 1994)) is 58 ms (blue open circle and Table 3.6) and the corresponding temperature-dependent relation (blue line) can be calculated assuming a Q_{10} of 2.4 (Miledi *et al.*, 1982). A straightforward quantitative information on the ensuing azimuthal movement of Tm back to the resting position in the thin filament is not available, because its time course is affected by the presence of actin-attached myosin motors. In fact, the half-time of the drop of the amplitude of AL2 after the end of stimulation from Kress *et al*. (1986) determined at 3.7 μm SL in the absence of filament overlap is 230 ms, , a value that is 300 ms less than the value determined at 2.2 μm SL during relaxation from the tetanic contraction.

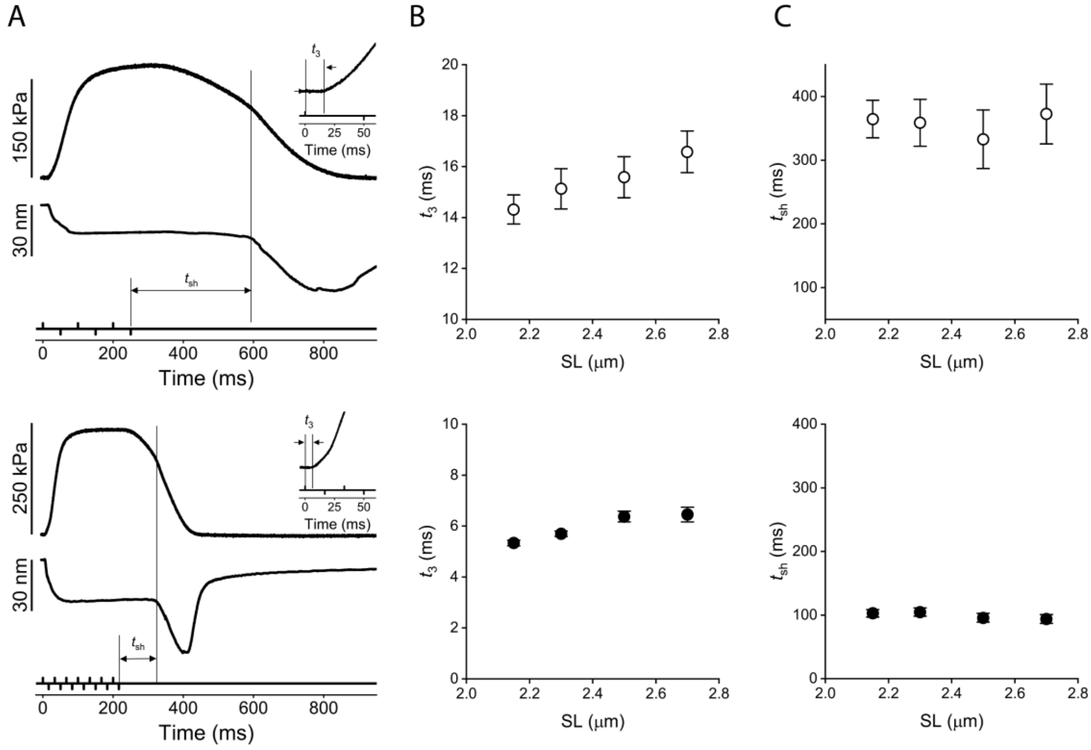

Fig. 3.10. Temperature and SL dependence of activation and relaxation of contraction. A. Upper panel 4 °C, lower panel 14 °C. In each panel upper trace is force, middle trace half-sarcomere length change, lower trace stimuli. The long vertical line marks the start of chaotic relaxation; the time elapsed from the last stimulus (short vertical line) indicated by the double arrowheads is tsh. In the insets the force trace of the corresponding panel is expanded to show t3. **B** and **C.** Relation between t_3 (B) and t_{sh} (C) and SL at 4 °C (open circles) and 14 °C (filled circles).

A signal for the OFF transition of thin filament structure collected at such extreme SL as 3.7 μm may be influenced by biassing effect on the time course of $[Ca^{2+}]_i$ decay (Miledi *et al.*, 1982) and does not represent a reliable parameter for the comparative plot in Fig. 3.9, B. In this respect, the use of PNB is the ideal tool to release the OFF transition in the thin filament structure from the influence of actin-attached motors. Under these conditions the switching OFF of the titin I-band spring can be related to

$[Ca^{2+}]_i$ decay as shown in Fig. 3.9, B by plotting $t_{L,OFF}$, the time following the first stimulus at which e_1 starts to decrease (black open circles, from Tables 3.5 and 3.6) and $t_{1/2,OFF}$, the time at which e_1 attains 50% recovery (black filled circles, from Tables 5 and 3.6) and drawing the grey shaded area, calculated with the relative Q_{10} (2.02), which defines the temperature dependence of the transition. Superimposing, on the plots of Fig. 3.9, B, the temperature dependence of $t_{sw,}$ (violet filled circles and line), the parameter that marks the OFF transition in terms of recovery of the large extensibility of the I-band titin spring at any SL (Tables 3.1-3.3), it can be seen how well it fits within the process defined by the 4 kHz oscillation at 3 μm SL. Once again, notwithstanding the different source of the data plotted in Fig. 3.9, B, it is impressive how strict and unique is the temporal relation between the relatively rapid time course of $[Ca^{2+}]_i$ decay (at 4 °C, $t_{1/2}$ ~60 ms) and the ensuing slower process of switching OFF I-band titin elasticity (that at 4 °C starts just at ~60 ms and proceeds with a $t_{1/2}$ of 220 ms).

The relaxation of the isometric force following the end of tetanic stimulation is even slower and accelerates only at a time after the last action potential at which the tension shows a shoulder (t_{sh}) (Huxley & Simmons, 1970). t_{sh} (marked by the vertical line in Fig. 3.10, A) is ~350 ms at 4 °C (upper panel). Before t_{sh} the relaxation is characterised by an isometric phase during which sarcomeres maintain a homogeneous, almost constant length (lower trace) and myofilaments maintain their ON structure, as measured by X-ray diffraction (Brunello *et al.*, 2009); at t_{sh} an accelerated chaotic phase of relaxation starts, in which some sarcomeres shorten and others give. t_{sh} shows a threefold reduction when temperature is increased to 14 °C (Fig. 3.10, A lower panel) and at either temperature is independent of SL (Fig. 13.10, C, upper panel 4°C, lower panel 14 °C, Table 3.6). The average values of t_{sh} at 4 °C (358 ± 19 ms) and at 14 °C (100 ± 3 ms), are reported in Fig 3.9, B (green circles) together with the temperature dependence of t_{sh} calculated for the whole temperature range (green line), making evident that t_{sh} follows with a large delay the switching OFF of I-band titin spring (grey shaded area and violet line). This is expected since the recovery of the resting I-band titin extensibility at any SL is the necessary condition for the transition to the chaotic and rapid phase of relaxation. However, a quantitative definition of the temporal sequence between the two processes is not possible because, following the end of stimulation in the presence of PNB and thus in the absence of actin attached motors, Tm movement back to the resting position is controlled solely by the relatively fast Ca^{2+}

decay and the ensuing titin detachment from actin and recovery of resting extensibility occur according to our measurements of the OFF transition of titin parameters (grey shaded area and violet line in Fig. 3.9, B).

On the other hand, following the end of tetanic stimulation in control, the presence of the actin attached motors delays the recovery of resting position of Tm along the thin filament with respect to Ca^{2+} drop (Caputo *et al.*, 1994), and, consequently, not only the relaxation of the contraction (green circles and line in Fig. 3.9, B), but also, presumably, the detachment of titin from actin and the recovery of resting extensibility.

Chapter 4. Discussion

4.1 How the dual state of titin bites into muscle contraction-relaxation

The classical explanation for the mechanism that counteracts the intrinsic instability of serially arranged half-sarcomeres foresees the contribution of I-band titin: as a spring in parallel with the array of motors in the A-band, I-band titin accounts for force equilibration of the lengthening weaker half-sarcomere using its stress-strain relation, which is identified, in a muscle fibre in the absence of the contribution of ECM, with the passive-force-SL relation (Fig. 1.2, B, triangles). However, passive force in a muscle fibre starts to rise at SL >2.5 µm and attains a significant fraction of tetanic force (10%) at SL ≥3 µm (Fig. 1.2, B)(Granzier & Wang, 1993; Trombitas *et al.*, 1998; Reconditi *et al.*, 2014; Linke, 2018; Meyer & Lieber, 2018), indicating that at physiological SL the underlying stiffness of titin is too low to prevent substantial lengthening of the weaker half-sarcomeres and development of SL inhomogeneity. Also the relatively small (~30%) increase by Ca^{2+} of static (Labeit *et al.*, 2003) or dynamic stiffness (Dutta *et al.*, 2018) of I-band titin elements found in vitro cannot suit the task.

In this work we find that upon stimulation, I-band titin switches from an OFF state, in which its mechanical contribution to the half-sarcomere is dominated by the large and SL-dependent extensibility of the proximal poly-Ig domain, to an ON state in which it exhibits a more elastic, SL independent, rigidity under stretch that in terms of stiffness (e_2) attains ~3 pN/nm per htf. How such a stiffness plays against the intrinsic instability of serially linked half-sarcomeres is exemplified here following. Let’s assume that in a muscle fibre stimulated to develop an isometric tetanus at the average SL of 2.5 µm a weak half-sarcomere undergoes a stress of 0.2 $T_{0,c}$ (or 50 pN per htf) because the strong half-sarcomere in series develops a force that exceeds by that amount the force capability of the weak one. The strain in the switched ON I-band titin spring of the weak half-sarcomere required for equilibration within the first 50 ms of contraction would be (50 pN/3 pN/nm =) 17 nm. In a tetanus of 500 ms duration, further strain would occur at a velocity of ≤10 nm/s per hs and thus would add no more than 5 nm per hs. At the end of the tetanus the length of the weak half-sarcomere would have increased by 22 nm. Thus, the average SL of the weak sarcomeres would have increased from 2.5 to 2.544 μm, that is by 1.7%.

A systematic investigation of the activation-dependent change of the I-band titin has not been conducted at 2.3 μm SL, at which the resting extensibility could not be determined for the saturation of loudspeaker-motor movement. However, a semi-quantitative evaluation of e_2 at 2.3 μm SL, which can be extracted from the response to a force step of 0.12 $T_{0,c}$ (grey trace in the left column of Figure3.4) indicates that it may be only slightly smaller than 3 pN/nm per htf. Thus, also at full filament overlap the I-band titin in the ON-state responds under stress with a strain comparable to that reported for 2.5 μm SL and above. This property finds a straightforward explanation in a mechanism that implies binding to actin of the region of the I-band titin proximal to the PEVK domain. In this way, independent of SL, the extensible proximal poly-Ig domain is excluded and the I-band titin spring reduces to the PEVK region (Figure 3.8,B and D). At 3 μm SL, notwithstanding the poly-Ig domain has likely attained its contour length (Figure 1.3, B, and Figure 4.1) and thus should provide little contribution to the extensibility of the I-band titin in the OFF-state, stimulation induces both a three times increase in e_2 and a shift from a more viscoelastic to a more elastic response to 4 kHz oscillation. Both these results indicate that the OFF-ON transition in the I-band titin implies not only the suppression of the proximal poly-Ig domain extensibility, but also a Ca^{2+}-dependent effect on the elasticity of the elements of the I-band titin distal to the N2A region. In this respect it must be noted that the threefold increase in e_2 at 3 μm SL cannot be accounted for by the much smaller (< 30%) Ca^{2+}-dependent increase in static stiffness of the I-band titin reported, together with the reduction in the persistence length of the PEVK domain, in combined *in situ* and *in vitro* experiments (Labeit *et al.*, 2003).

Two other relevant issues emerge when the active titin properties discovered here are reflected on the physiology of muscle. The first derives from the finding that in the active muscle fibre the maximum velocity of shortening V_0 remains constant in the SL range 2.7-1.8 μm (Edman, 1979). This can be accommodated with the proposed mechanism for active titin elasticity only by assuming that the titin-actin bond has rectifying properties: it resists to lengthening, but is quite dynamic when stressed in the shortening direction, as it happens during active shortening, so that it does not represent a significant load whatever are the SL and the amount of shortening. The second issue emerges in relation to the acceleration of the relaxation from an isometric tetanus. During the slow isometric phase of relaxation the $[Ca^{2+}]_i$ has already dropped near resting values (Caputo *et al.*, 1994) and myosin motors detach very slowly as estimated by the slow decay of force (Figure 3.9, B) and stiffness (Brunello *et al.*, 2009). This can be explained by considering that motor detachment is strain dependent and, in this phase, attached motors are on average slightly more strained than during the preceding phase of tetanic contraction as a consequence of the recoil of the series elasticity accompanying the slow force decay (Brunello *et al.*, 2009). The transition to chaotic phase that allows a rapid conclusion of the relaxation is likely triggered by the first half-sarcomeres in which attached motors attain the critical level of strain at which rapid detachment occurs (Lombardi & Piazzesi, 1990). In the absence of Ca^{2+}, following motor detachment Tm moves back to its resting position and the detached motors cannot reattach and support the force exerted by the half-sarcomeres in which motors are still attached. The ensuing shortening in these half-sarcomeres speeds up motor detachment and completion of the chemo-mechanical cycle. This description of the mechanism of relaxation indicates that chaotic relaxation is necessary to rapidly end the contraction, as required for the execution of coordinated movement by antagonist muscles. The finding that switched ON I-band titin resists stretch with a stiffness of 3 pN/nm implies, as a necessary condition for the chaotic relaxation to occur, that it is preceded by the titin switching to the OFF state. This temporal sequence is verified in Figure 3.9, where the time for the shoulder (t_{sh}, green circles and dashed line) follows the time for the OFF transition of titin parameters, namely the recovery of resting viscoelasticity, as measured by the drop of e_1 at 3 μm SL (grey shaded area), and the recovery of resting extensibility at any SL, as measured by t_{sw} (violet dashed line).

4.2 Relation with existing *in situ* and *in vitro* studies on titin mechanics

The rise of an elastic element different from myosin motors during muscle contraction was suggested by stiffness measurements early following the stimulation of single fibres from frog skeletal muscle (Bagni *et al.*, 2002; Bagni *et al.*, 2005; Colombini *et al.*, 2010; Fusi *et al.*, 2014a) and confirmed in both intact (Nocella *et al.*, 2012) and skinned mammalian muscle preparations (Cornachione & Rassier, 2012; Percario *et al.*, 2018). However, a quantitative description of the I-band titin spring *in* *situ* in the active sarcomere was hampered by the presence, in the A-band in parallel with the I-band titin, of myosin motors that contribute to the mechanical response with their dynamic stiffness (Huxley & Simmons, 1971) and detachment/attachment kinetics (Lombardi & Piazzesi, 1990). Experiments conducted at extremely large SL to suppress the contribution of myosin motors (Leonard & Herzog, 2010; Powers *et al.*, 2014) did not provide physiologically reliable information. Earlier work on Ca^{2+}-activated demembranated rabbit psoas fibres succeeded in eliminating the contribution of the A-band elastic elements by removing the actin filament with gelsolin (Granzier & Wang, 1993). However, the remaining I-band elasticity showed a Young modulus of 0.1 MPa, more than ten times smaller than that based on the stiffness of the parallel elasticity found in intact fibre experiments (Fusi *et al.*, 2014a). The limits due to the dominant contribution of the A-band elements have been mitigated by measuring half-sarcomere stiffness with small 4 kHz oscillations imposed on single frog muscle fibres early during isometric force development, when the number of attached motors is small (Powers *et al.*, 2020). The active I-band stiffness estimated at different SL under these conditions provided the constraints for fitting a complete mechanical model of the half-sarcomere (Pertici *et al.*, 2019; Powers *et al.*, 2020). In relatively good agreement with the results of the present work, it was found that the I-band titin spring starts to give a significant contribution to half-sarcomere elasticity above 2.7 μm SL, with an undamped stiffness of 6 pN/nm per htf that is constant independent of SL. The limit of that work was the impossibility to define the kinetics of I-band titin relaxation in response to a force step, preventing from the description of the dynamic interface between I-band titin and A-band myosin motors that is relevant during contraction. However an interface was generated by integrating the undamped stiffness with the titin structural dynamics defined with *in vitro* single-molecule mechanics, exploiting the evidence from both AFM and optical tweezers that titin-Ig domains can be mechanically unfolded (Kellermayer *et al.*, 1997; Rief *et al.*, 1997; Tskhovrebova *et al.*, 1997). Accordingly, the gap between the undamped I-band titin stiffness and the two orders-of-magnitude smaller static stiffness responsible for the passive force–SL relation was filled introducing the relaxation kinetics derived from Ig domains' folding–unfolding dynamics ((Martonfalvi *et al.*, 2014; Rivas-Pardo *et al.*, 2016)).

Taking into account the load dependent kinetics of the Ig-folding-unfolding reaction defined in those experiments it was possible to calculate a dynamic resistance that in the weaker half-sarcomeres equilibrated the force of the stronger half-sarcomeres with a lengthening that was smaller than that expected if the equilibration were due to the static stiffness. Within the few hundred milliseconds of the contraction, the half-sarcomere lengthening resulted as large as a few hundred nanometres (Powers *et al.*, 2020). Otherwise, the results in the present paper show that the I-band titin lengthening necessary for force equilibration is ten times smaller (a few tens of nanometers) and is not due to a dynamic resistance but rather to the rise of an almost static strain in the I-band titin spring that is quite small in the ON state. Another limit of the mechanism hypothesised in Powers *et al.* (2020) becomes evident considering that, at the SL's within the working range of skeletal muscles (2.1 - 2.6 μm), the extensibility of the I-band titin at rest is substantially based on the straightening out of randomly bent elements of the proximal poly-Ig domain (Linke *et al.*, 1998a; Linke *et al.*, 1998b; Minajeva *et al.*, 2001), and only at SL above 2.8-3 μm (at which the contour length of the proximal poly-Ig domain is attained) unfolding of Ig elements becomes relevant in the response to an increase in stress (Granzier *et al.*, 1996; Linke *et al.*, 1996; Trombitas *et al.*, 1998).

In this work we assume that the passive force-SL relation of the single fibre from frog skeletal muscle can be explained by the contribution of two spring elements with different extensibility, serially linked in the I-band titin: (*i*) the proximal poly-Ig domain that in the SL range 2-2.7 μm behaves as an entropic spring with a large persistence length (L_p) and thus responds to a stretch with straightening of its bent elements with development of very low force, and (*ii*) the PEVK domain which, at SL ≥2.8 μm, at which the poly-Ig spring attains its contour length (L_c) becoming inextensible, responds to further stretch with rise in force according to an L_p that is much shorter than that of the poly-Ig spring. In the absence of direct information on the molecular structure of the frog titin, this molecular explanation of the passive force-SL relation relies on the definition of the contributions of the two spring elements to the I-band titin in the rat psoas myofibril (Linke *et al.*, 1998a). Justifications for the assumption are that (*i*) in both the single fibre from frog tibialis anterior and the myofibril from rat psoas the passive force-SL relation is free from the contribution of the ECM and thus depends uniquely on I-band titin ((Meyer & Lieber, 2018)), and (ii) the titin structure is mostly conserved in ortholog isoforms of the fast skeletal muscle of vertebrates. The assumption is tested here by conducting a comparative analysis of the force – SL relation of the two experimental models (Figure 4.1, blue circles rat psoas myofibril from (Linke *et al.*, 1998a), red circles frog muscle fibre from Figure 1.2, B).

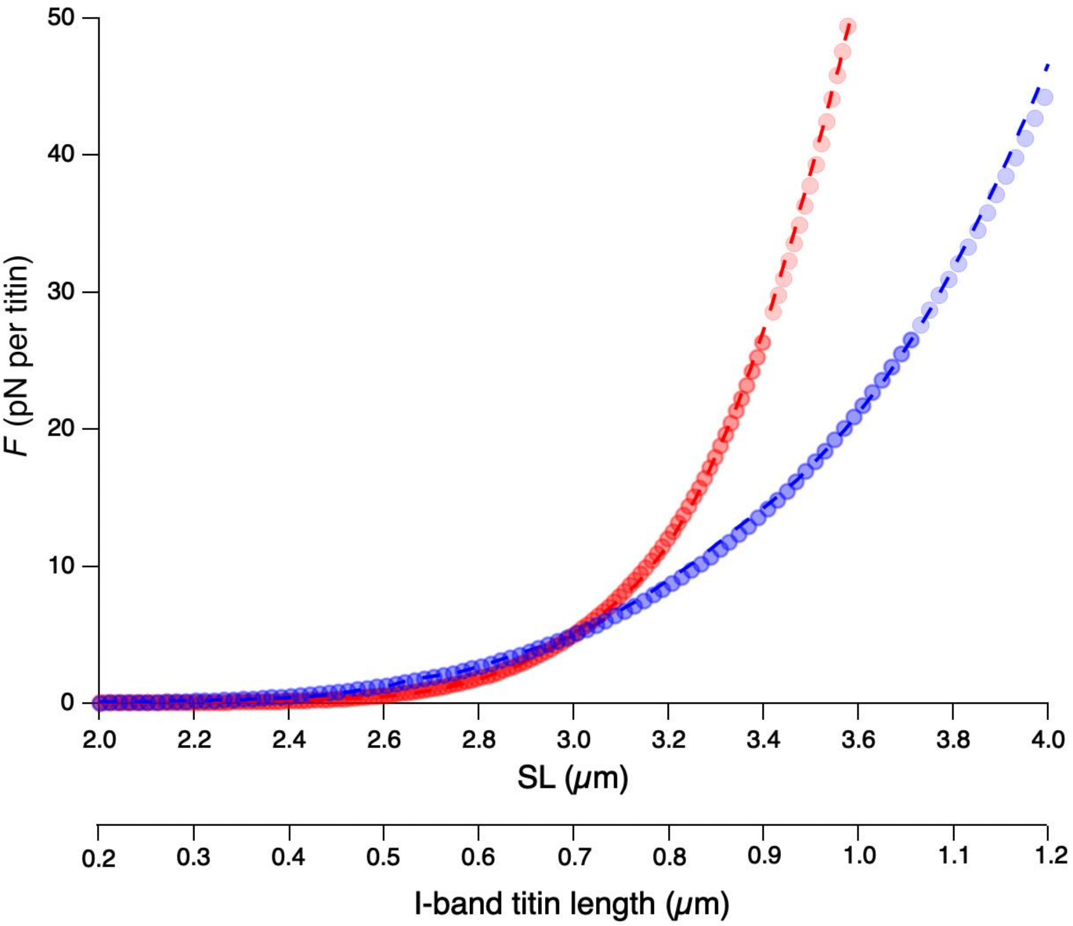

Figure 4.1. Passive force-SL relation and its simulation by serially linked poly-Ig and PEVK domains. The circles are the fit to the experimental relations of frog muscle fibre (red, from Figure 2.1 B) and of rat psoas myofibril (blue, from (Linke *et al.*, 1998a)). The dashed lines are the result of the simulation obtained assuming the sequential extension of two WLC's, the WLC describing the poly-Ig domain elasticity and the WLC integrated by an enthalpic contribution describing the PEVK domain elasticity. As shown in Table 4.1 the main difference in the simulation parameters is the Young modulus of the enthalpic contribution that is 80% larger in the frog.

These two preparations share the same myosin filament length (l_M = 1.6 μm) and therefore the force - SL relation can be uniquely expressed also as force versus the I-band titin length (l_{TI}= (SL – l_M)/2) (lower abscissa). It can be seen that the two relations exhibit a quite similar large extensibility up to SL ~2.8 μm and then diverge with the frog fibre relation rising more steeply. This qualitative comparison suggests that (*i*) within 2.8 μm SL in either case the elasticity of the I-band titin is dominated by the poly-Ig entropic elasticity with a similar large L_p; (*ii*) at larger SL's, where the enthalpic component of the PEVK elasticity becomes important (Linke *et al.*, 1998b; Trombitas *et al.*, 1998), the frog titin exhibits a larger Young modulus (*E*).

For a quantitative test we used the model of the I-band titin elasticity that implies the sequential extension of two serially linked WLC's to fit the force-SL relation (Labeit & Kolmerer, 1995; Linke *et al.*, 1996; Trombitas *et al.*, 1998): the first WLC is provided by the poly-Ig segment with a purely entropic elasticity (with L_p = 42 nm for the psoas myofibril according to (Linke *et al.*, 1998a) and the second provided by the PEVK segment with entropic and enthalpic elasticities (with L_p = 1.2 nm and E = 185 pN, respectively, for the psoas myofibril according to (Linke *et al.*, 1998b).

SL (μm)	I-band titin length (μm)	L_p (μm)	L_c (μm)	E (pN)
Rat psoas myofibril				
<2.8	<0.6 (poly-Ig)	0.031 ± 0.011	0.66 ± 0.01	-
>2.8	>0.6 (PEVK)	0.0013 ± 0.00004	1.05 ± 0.08	193 ± 5.6
Frog muscle fibre				
<2.8	< 0.6 (poly-Ig)	0.042 ± 0.001	0.68 ± 0.03	-
>3.0	>0.6 (PEVK)	0.0028 ± 0.00008	0.91 ± 0.04	331± 9.6

Table 4.1. Parameters of the I-band titin model.

Our fit to the psoas myofibril relation (dashed blue line in Figure 4.1) gives almost the same estimates of the relevant parameters of the model as in the original works (Table 4.1), indicating the reliability of our simulation procedure. When the same procedure is applied to simulate the frog fibre relation (dashed red line in 4.1), the values of L_p of the poly-Ig segment and of the PEVK segment estimated by the fit are 42 nm and 2.8 nm respectively and the estimated value of E is 331 pN (Table 4.1). The comparative analysis demonstrates that in either preparation the large extensibility of the I-band titin, due to the entropic elasticity of the poly-Ig domain, attains its limit at ~3 μm SL.

Chapter 5. Conclusions

A precedently inconceivable efficiency of the half-sarcomere design based on the complementary roles of the A and I band emerges from the present work. The collective myosin motor in the A-band is responsible for the steady production of force and power in isometric and isotonic contractions and for the resistance to forcible lengthening in eccentric contractions; titin in the I-band serves a dual function through a Ca^{2+}-dependent switch between two states: (*i*) at rest (OFF state), titin exhibits the large extensibility admitted by the randomly oriented elements of the proximal poly-Ig domain to adapt the half-sarcomere length to the physiological range of muscle lengths; (*ii*) following Ca^{2+}-dependent thin filament activation, at whatever SL, the I-band titin acquires rectifying properties: while it allows unloaded shortening at the maximum velocity, it opposes lengthening with a stiffness of 3 pN nm^{-1} per htf (ON state), in this way preserving the half-sarcomere from the intrinsic instability of serially linked A-band force generators.

At the same time the conclusions of this work open new scenarios for the investigation of the molecular basis of muscle regulatory mechanisms and related functions: (*i*) the first detailed quantitative description of the ON state of the I-band titin and the identification of its control with the Ca^{2+}-dependent thin filament activation that makes actin available for binding of the N2A domain provide a new basis for *in situ* and *in vitro* investigations of the mechanical and signaling pathways that link the N2A domain to muscle hypertrophy and thermoregulation and of the chain of events that link the N2A mutations to disease (Nishikawa *et al.*, 2020); (*ii*) the SL-independent high stiffness with rectifying property that characterizes the ON state of the I-band titin could provide the effective mechanical link for an A-band titin role in the mechano-sensing-based regulation of the thick filament (Piazzesi *et al.*, 2018).

References

Anderson BR & Granzier HL. (2012). Titin-based tension in the cardiac sarcomere: molecular origin and physiological adaptations. *Prog Biophys Mol Biol* **110,** 204-217.

Bagni MA, Cecchi G & Colombini B. (2005). Crossbridge properties investigated by fast ramp stretching of activated frog muscle fibres. *J Physiol (London)* **565,** 261-268.

Bagni MA, Cecchi G, Colombini B & Colomo F. (2002). A non-cross-bridge stiffness in activated frog muscle fibers. *Biophys J* **82,** 3118-3127.

Barclay CJ, Woledge RC & Curtin NA. (2010). Inferring crossbridge properties from skeletal muscle energetics. *Prog Biophys Mol Biol* **102,** 53-71.

Bennett P, Rees M & Gautel M. (2020). The Axial Alignment of Titin on the Muscle Thick Filament Supports Its Role as a Molecular Ruler. *J Mol Biol* **432,** 4815-4829.

Bennett PM, Hodkin TE & Hawkins C. (1997). Evidence that the tandem Ig domains near the end of the muscle thick filament form an inelastic part of the I-band titin. *J Struct Biol* **120,** 93-104.

Bianco P, Bongini L, Melli L, Falorsi G, Salvi L, Cojoc D & Lombardi V. (2014). Fast Force Clamp in Optical Tweezers: A Tool to Study the Kinetics of Molecular Reactions, pp. 123-147. Springer Berlin Heidelberg, Berlin, Heidelberg.

Bianco P, Nagy A, Kengyel A, Szatmari D, Martonfalvi Z, Huber T & Kellermayer MS. (2007). Interaction forces between F-actin and titin PEVK domain measured with optical tweezers. *Biophys J* **93,** 2102-2109.

Brunello E, Bianco P, Piazzesi G, Linari M, Reconditi M, Panine P, Narayanan T, Helsby WI, Irving M & Lombardi V. (2006). Structural changes in the myosin filament and cross-bridges during active force development in single intact frog muscle fibres: stiffness and X-ray diffraction measurements. *J Physiol (London)* **577,** 971-984.

Brunello E, Fusi L, Reconditi M, Linari M, Bianco P, Panine P, Narayanan T, Piazzesi G, Lombardi V & Irving M. (2009). Structural changes in myosin motors and filaments during relaxation of skeletal muscle. *J Physiol (London)* **587,** 4509-4521.

Cambridge EW & Haines J. (1959). A new versatile transducer system. *J Physiol (London)* **149,** 2-3P.

Caputo C, Edman KA, Lou F & Sun YB. (1994). Variation in myoplasmic Ca2+ concentration during contraction and relaxation studied by the indicator fluo-3 in frog muscle fibres. *J Physiol (London)* **478 (Pt 1),** 137-148.

Caremani M, Fusi L, Linari M, Reconditi M, Piazzesi G, Irving TC, Narayanan T, Irving M, Lombardi V & Brunello E. (2021). Dependence of thick filament structure in relaxed mammalian skeletal muscle on temperature and interfilament spacing. *J Gen Physiol* **153**.

Cecchi G. (1983). A circuit specially suited for use with high-frequency capacitance gauge force transducers. *Arch Ital Biol* **121,** 215-217.

Cecchi G, Colomo F, Lombardi V & Piazzesi G. (1987). Stiffness of frog muscle fibres during rise of tension and relaxation in fixed-end or length-clamped tetani. *Pflugers Arch* **409,** 39-46.

Colombini B, Nocella M, Benelli G, Cecchi G & Bagni MA. (2010). Cross-bridge properties in single intact frog fibers studied by fast stretches. *Adv Exp Med Biol* **682,** 191-205.

Cornachione AS & Rassier DE. (2012). A non-cross-bridge, static tension is present in permeabilized skeletal muscle fibers after active force inhibition or actin extraction. *Am J Physiol Cell Physiol* **302,** C566-574.

Dobbie I, Linari M, Piazzesi G, Reconditi M, Koubassova N, Ferenczi MA, Lombardi V & Irving M. (1998). Elastic bending and active tilting of myosin heads during muscle contraction. *Nature* **396,** 383-387.

Dutta S, Tsiros C, Sundar SL, Athar H, Moore J, Nelson B, Gage MJ & Nishikawa K. (2018). Calcium increases titin N2A binding to F-actin and regulated thin filaments. *Scientific reports* **8,** 14575.

Ebashi S, Endo M & Otsuki I. (1969). Control of muscle contraction. *Q Rev Biophys* **2,** 351-384.

Edman KA. (1979). The velocity of unloaded shortening and its relation to sarcomere length and isometric force in vertebrate muscle fibres. *J Physiol (London)* **291,** 143-159.

Eusebi F & Miledi R. (1983). Divalent cations and temperature dependent block of impulse propagation at the frog neuromuscular junction. *Muscle Nerve* **6,** 602-605.

Ford LE, Huxley AF & Simmons RM. (1977). Tension responses to sudden length change in stimulated frog muscle fibres near slack length. *J Physiol (London)* **269,** 441-515.

Freiburg A, Trombitas K, Hell W, Cazorla O, Fougerousse F, Centner T, Kolmerer B, Witt C, Beckmann JS, Gregorio CC, Granzier H & Labeit S. (2000). Series of exon-skipping events in the elastic spring region of titin as the structural basis for myofibrillar elastic diversity. *Circ Res* **86,** 1114-1121.

Furst DO, Osborn M, Nave R & Weber K. (1988). The organization of titin filaments in the half-sarcomere revealed by monoclonal antibodies in immunoelectron microscopy: a map of ten nonrepetitive epitopes starting at the Z line extends close to the M line. *J Cell Biol* **106,** 1563-1572.

Fusi L, Brunello E, Reconditi M, Piazzesi G & Lombardi V. (2014a). The non-linear elasticity of the muscle sarcomere and the compliance of myosin motors. *J Physiol (London)* **592,** 1109-1118.

Fusi L, Brunello E, Sevrieva IR, Sun YB & Irving M. (2014b). Structural dynamics of troponin during activation of skeletal muscle. *Proc Natl Acad Sci USA* **111,** 4626-4631.

Fusi L, Percario V, Brunello E, Caremani M, Bianco P, Powers JD, Reconditi M, Lombardi V & Piazzesi G. (2017). Minimum number of myosin motors accounting for shortening velocity under zero load in skeletal muscle. *J Physiol (London)* **595,** 1127-1142.

Gautel M & Djinovic-Carugo K. (2016). The sarcomeric cytoskeleton: from molecules to motion. *J Exp Biol* **219,** 135-145.

Gordon AM, Homsher E & Regnier M. (2000). Regulation of contraction in striated muscle. *Physiol Rev* **80,** 853-924.

Gordon AM, Huxley AF & Julian FJ. (1966). The variation in isometric tension with sarcomere length in vertebrate muscle fibres. *J Physiol (London)* **184,** 170-192.

Granzier H, Helmes M & Trombitas K. (1996). Nonuniform elasticity of titin in cardiac myocytes: a study using immunoelectron microscopy and cellular mechanics. *Biophys J* **70,** 430-442.

Granzier H & Labeit S. (2002). Cardiac titin: an adjustable multi-functional spring. *J Physiol (London)* **541,** 335-342.

Granzier HL & Wang K. (1993). Passive tension and stiffness of vertebrate skeletal and insect flight muscles: the contribution of weak cross-bridges and elastic filaments. *Biophys J* **65,** 2141-2159.

Hanson J & Huxley HE. (1957). Quantitative studies on the structure of cross-striated myofibrils. II. Investigations by biochemical techniques. *Biochim Biophys Acta* **23,** 250-260.

Haugen P. (1982). The dependence of the latency relaxation on temperature in single muscle fibres of the frog. *Acta Physiol Scand* **114,** 179-186.

Herron TJ, Korte FS & McDonald KS. (2001). Power output is increased after phosphorylation of myofibrillar proteins in rat skinned cardiac myocytes. *Circ Res* **89,** 1184-1190.

Hidalgo C & Granzier H. (2013). Tuning the molecular giant titin through phosphorylation: role in health and disease. *Trends Cardiovasc Med* **23,** 165-171.

Hooijman P, Stewart MA & Cooke R. (2011). A new state of cardiac myosin with very slow ATP turnover: a potential cardioprotective mechanism in the heart. *Biophys J* **100,** 1969-1976.

Horowits R, Kempner ES, Bisher ME & Podolsky RJ. (1986). A physiological role for titin and nebulin in skeletal muscle. *Nature* **323,** 160-164.

Horowits R & Podolsky RJ. (1987). The positional stability of thick filaments in activated skeletal muscle depends on sarcomere length: evidence for the role of titin filaments. *J Cell Biol* **105,** 2217-2223.

Huxley AF. (1957). Muscle structure and theories of contraction. *Prog Biophys Biophys Chem* **7,** 255-318.

Huxley AF. (1973). A note suggesting that the cross-bridge attachment during muscle contraction may take place in two stages. *Proc R Soc Lond B Biol Sci* **183,** 83-86.

Huxley AF & Lombardi V. (1980). A sensitive force transducer with resonant frequency 50 kHz. *J Physiol (London)* **305,** 15-16P.

Huxley AF, Lombardi V & Peachey LD. (1981). A system for fast recording of longitudinal displacement of a striated muscle fibre. *J Physiol (London)* **317,** 12P-13P.

Huxley AF & Simmons RM. (1970). Rapid 'give' and the tension 'shoulder' in the relaxation of frog muscle fibres. *J Physiol (London)* **210,** 32P-33P.

Huxley AF & Simmons RM. (1971). Proposed mechanism of force generation in striated muscle. *Nature* **233,** 533-538.

Huxley H, Reconditi M & Irving T. (2009). New X-ray Data about Myosin-binding Protein C in Frog Muscle. *Biophys J* **96,** 616a-616a.

Huxley HE. (1969). The mechanism of muscular contraction. *Science* **164,** 1356-1365.

Huxley HE & Brown W. (1967). The low-angle x-ray diagram of vertebrate striated muscle and its behaviour during contraction and rigor. *J Mol Biol* **30,** 383-434.

Huxley HE & Hanson J. (1957). Quantitative studies on the structure of cross-striated myofibrils. I. Investigations by interference microscopy. *Biochim Biophys Acta* **23,** 229-249.

Itoh Y, Suzuki T, Kimura S, Ohashi K, Higuchi H, Sawada H, Shimizu T, Shibata M & Maruyama K. (1988). Extensible and less-extensible domains of connectin filaments in stretched vertebrate skeletal muscle sarcomeres as detected by immunofluorescence and immunoelectron microscopy using monoclonal antibodies. *J Biochem* **104,** 504-508.

Julian FJ & Morgan DL. (1979). The effect on tension of non-uniform distribution of length changes applied to frog muscle fibres. *J Physiol (London)* **293,** 379-392.

Jung HS, Burgess SA, Billington N, Colegrave M, Patel H, Chalovich JM, Chantler PD & Knight PJ. (2008). Conservation of the regulated structure of folded myosin 2 in species separated by at least 600 million years of independent evolution. *Proc Natl Acad Sci USA* **105,** 6022-6026.

Kampourakis T, Sun YB & Irving M. (2016). Myosin light chain phosphorylation enhances contraction of heart muscle via structural changes in both thick and thin filaments. *Proc Natl Acad Sci USA* **113,** E3039-3047.

Kellermayer MS, Smith SB, Granzier HL & Bustamante C. (1997). Folding-unfolding transitions in single titin molecules characterized with laser tweezers. *Science* **276,** 1112-1116.

Kontrogianni-Konstantopoulos A & Bloch RJ. (2003). The hydrophilic domain of small ankyrin-1 interacts with the two N-terminal immunoglobulin domains of titin. *J Biol Chem* **278,** 3985-3991.

Kovacs M, Toth J, Hetenyi C, Malnasi-Csizmadia A & Sellers JR. (2004). Mechanism of blebbistatin inhibition of myosin II. *J Biol Chem* **279,** 35557-35563.

Kress M, Huxley HE, Faruqi AR & Hendrix J. (1986). Structural changes during the activation of frog muscle studied by time-resolved x-ray diffraction. *J Mol Biol* **188,** 325.

Kumar M, Govindan S, Zhang M, Khairallah RJ, Martin JL, Sadayappan S & de Tombe PP. (2015). Cardiac Myosin-binding Protein C and Troponin-I Phosphorylation Independently Modulate Myofilament Length-dependent Activation. *J Biol Chem* **290,** 29241-29249.

Labeit D, Watanabe K, Witt C, Fujita H, Wu Y, Lahmers S, Funck T, Labeit S & Granzier H. (2003). Calcium-dependent molecular spring elements in the giant protein titin. *Proc Natl Acad Sci USA* **100,** 13716-13721.

Labeit S, Gautel M, Lakey A & Trinick J. (1992). Towards a molecular understanding of titin. *EMBO J* **11,** 1711-1716.

Labeit S & Kolmerer B. (1995). Titins: giant proteins in charge of muscle ultrastructure and elasticity. *Science* **270,** 293-296.

Lange S, Auerbach D, McLoughlin P, Perriard E, Schafer BW, Perriard JC & Ehler E. (2002). Subcellular targeting of metabolic enzymes to titin in heart muscle may be mediated by DRAL/FHL-2. *J Cell Sci* **115,** 4925-4936.

Leonard TR & Herzog W. (2010). Regulation of muscle force in the absence of actin-myosin-based cross-bridge interaction. *Am J Physiol Cell Physiol* **299,** C14-20.

Limouze J, Straight AF, Mitchison T & Sellers JR. (2004). Specificity of blebbistatin, an inhibitor of myosin II. *J Muscle Res Cell Motil* **25,** 337-341.

Linari M, Brunello E, Reconditi M, Fusi L, Caremani M, Narayanan T, Piazzesi G, Lombardi V & Irving M. (2015). Force generation by skeletal muscle is controlled by mechanosensing in myosin filaments. *Nature* **528,** 276-279.

Linari M, Lucii L, Reconditi M, Casoni ME, Amenitsch H, Bernstorff S, Piazzesi G & Lombardi V. (2000). A combined mechanical and X-ray diffraction study of stretch potentiation in single frog muscle fibres. *J Physiol (London)* **526 Pt 3,** 589-596.

Linke WA. (2018). Titin Gene and Protein Functions in Passive and Active Muscle. *Annu Rev Physiol* **80,** 389-411.

Linke WA, Ivemeyer M, Mundel P, Stockmeier MR & Kolmerer B. (1998a). Nature of PEVK-titin elasticity in skeletal muscle. *Proc Natl Acad Sci USA* **95,** 8052-8057.

Linke WA, Ivemeyer M, Olivieri N, Kolmerer B, Ruegg JC & Labeit S. (1996). Towards a molecular understanding of the elasticity of titin. *J Mol Biol* **261,** 62-71.

Linke WA, Stockmeier MR, Ivemeyer M, Hosser H & Mundel P. (1998b). Characterizing titin's I-band Ig domain region as an entropic spring. *J Cell Sci* **111 (Pt 11),** 1567-1574.

Lombardi V & Menchetti G. (1984). The maximum velocity of shortening during the early phases of the contraction in frog single muscle fibres. *J Muscle Res Cell Motil* **5,** 503-513.

Lombardi V & Piazzesi G. (1990). The contractile response during steady lengthening of stimulated frog muscle fibres. *J Physiol (London)* **431,** 141-171.

Luther PK, Winkler H, Taylor K, Zoghbi ME, Craig R, Padron R, Squire JM & Liu J. (2011). Direct visualization of myosin-binding protein C bridging myosin and actin filaments in intact muscle. *Proc Natl Acad Sci USA* **108,** 11423-11428.

Lymn RW & Taylor EW. (1971). Mechanism of adenosine triphosphate hydrolysis by actomyosin. *Biochemistry* **10,** 4617-4624.

Ma K & Wang K. (2002). Interaction of nebulin SH3 domain with titin PEVK and myopalladin: implications for the signaling and assembly role of titin and nebulin. *FEBS Lett* **532,** 273-278.

Ma W, Gong H, Kiss B, Lee EJ, Granzier H & Irving T. (2018). Thick-Filament Extensibility in Intact Skeletal Muscle. *Biophys J* **115,** 1580-1588.

Magid A & Law DJ. (1985). Myofibrils bear most of the resting tension in frog skeletal muscle. *Science* **230,** 1280-1282.

Martonfalvi Z, Bianco P, Linari M, Caremani M, Nagy A, Lombardi V & Kellermayer M. (2014). Low-force transitions in single titin molecules reflect a memory of contractile history. *J Cell Sci* **127,** 858-870.

Maruyama K, Kimura S, Kuroda M & Handa S. (1977). Connectin, an elastic protein of muscle. Its abundance in cardiac myofibrils. *J Biochem* **82,** 347-350.

Matsuo T & Yagi N. (2008). Structural changes in the muscle thin filament during contractions caused by single and double electrical pulses. *J Mol Biol* **383,** 1019-1036.

Meyer G & Lieber RL. (2018). Muscle fibers bear a larger fraction of passive muscle tension in frogs compared with mice. *J Exp Biol* **221**.

Miledi R, Parker I & Zhu PH. (1982). Calcium transients evoked by action potentials in frog twitch muscle fibres. *J Physiol (London)* **333,** 655-679.

Minajeva A, Kulke M, Fernandez JM & Linke WA. (2001). Unfolding of titin domains explains the viscoelastic behavior of skeletal myofibrils. *Biophys J* **80,** 1442-1451.

Mulieri LA. (1972). The dependence of the latency relaxation on sarcomere length and other characteristics of isolated muscle fibres. *J Physiol (London)* **223,** 333-354.

Neagoe C, Opitz CA, Makarenko I & Linke WA. (2003). Gigantic variety: expression patterns of titin isoforms in striated muscles and consequences for myofibrillar passive stiffness. *J Muscle Res Cell Motil* **24,** 175-189.

Nishikawa K, Lindstedt SL, Hessel A & Mishra D. (2020). N2A Titin: Signaling Hub and Mechanical Switch in Skeletal Muscle. *Int J Mol Sci* **21**.

Nocella M, Colombini B, Bagni MA, Bruton J & Cecchi G. (2012). Non-crossbridge calcium-dependent stiffness in slow and fast skeletal fibres from mouse muscle. *J Muscle Res Cell Motil* **32,** 403-409.

Percario V, Boncompagni S, Protasi F, Pertici I, Pinzauti F & Caremani M. (2018). Mechanical parameters of the molecular motor myosin II determined in permeabilised fibres from slow and fast skeletal muscles of the rabbit. *J Physiol (London)* **596,** 1243-1257.

Pertici I, Caremani M & Reconditi M. (2019). A mechanical model of the half-sarcomere which includes the contribution of titin. *J Muscle Res Cell Motil* **40,** 29-41.

Peterson KJ, Lyons JB, Nowak KS, Takacs CM, Wargo MJ & McPeek MA. (2004). Estimating metazoan divergence times with a molecular clock. *Proc Natl Acad Sci USA* **101,** 6536-6541.

Piazzesi G, Caremani M, Linari M, Reconditi M & Lombardi V. (2018). Thick Filament Mechano-Sensing in Skeletal and Cardiac Muscles: A Common Mechanism

Able to Adapt the Energetic Cost of the Contraction to the Task. *Frontiers in physiology* **9,** 736.

Piazzesi G, Reconditi M, Dobbie I, Linari M, Boesecke P, Diat O, Irving M & Lombardi V. (1999). Changes in conformation of myosin heads during the development of isometric contraction and rapid shortening in single frog muscle fibres. *J Physiol (London)* **514 (Pt 2),** 305-312.

Piazzesi G, Reconditi M, Linari M, Lucii L, Bianco P, Brunello E, Decostre V, Stewart A, Gore DB, Irving TC, Irving M & Lombardi V. (2007). Skeletal muscle performance determined by modulation of number of myosin motors rather than motor force or stroke size. *Cell* **131,** 784-795.

Piazzesi G, Reconditi M, Linari M, Lucii L, Sun YB, Narayanan T, Boesecke P, Lombardi V & Irving M. (2002). Mechanism of force generation by myosin heads in skeletal muscle. *Nature* **415,** 659-662.

Pinto A, Sanchez F, Alamo L & Padron R. (2012). The myosin interacting-heads motif is present in the relaxed thick filament of the striated muscle of scorpion. *J Struct Biol* **180,** 469-478.

Powers JD, Bianco P, Pertici I, Reconditi M, Lombardi V & Piazzesi G. (2020). Contracting striated muscle has a dynamic I-band spring with an undamped stiffness 100 times larger than the passive stiffness. *J Physiol (London)* **598,** 331-345.

Powers K, Schappacher-Tilp G, Jinha A, Leonard T, Nishikawa K & Herzog W. (2014). Titin force is enhanced in actively stretched skeletal muscle. *J Exp Biol* **217,** 3629-3636.

Rayment I, Holden HM, Whittaker M, Yohn CB, Lorenz M, Holmes KC & Milligan RA. (1993a). Structure of the actin-myosin complex and its implications for muscle contraction. *Science* **261,** 58-65.

Rayment I, Rypniewski WR, Schmidt-Base K, Smith R, Tomchick DR, Benning MM, Winkelmann DA, Wesenberg G & Holden HM. (1993b). Three-dimensional structure of myosin subfragment-1: a molecular motor. *Science* **261,** 50-58.

Reconditi M, Brunello E, Fusi L, Linari M, Martinez MF, Lombardi V, Irving M & Piazzesi G. (2014). Sarcomere-length dependence of myosin filament structure in skeletal muscle fibres of the frog. *J Physiol (London)* **592,** 1119-1137.

Reconditi M, Brunello E, Linari M, Bianco P, Narayanan T, Panine P, Piazzesi G, Lombardi V & Irving M. (2011). Motion of myosin head domains during activation and force development in skeletal muscle. *Proc Natl Acad Sci USA* **108,** 7236-7240.

Reconditi M, Caremani M, Pinzauti F, Powers JD, Narayanan T, Stienen GJ, Linari M, Lombardi V & Piazzesi G. (2017). Myosin filament activation in the heart is tuned to the mechanical task. *Proc Natl Acad Sci USA* **114,** 3240-3245.

Reconditi M, Fusi L, Caremani M, Brunello E, Linari M, Piazzesi G, Lombardi V & Irving M. (2019). Thick Filament Length Changes in Muscle Have Both Elastic and Structural Components. *Biophys J* **116,** 983-984.

Reconditi M, Linari M, Lucii L, Stewart A, Sun YB, Boesecke P, Narayanan T, Fischetti RF, Irving T, Piazzesi G, Irving M & Lombardi V. (2004). The myosin motor in muscle generates a smaller and slower working stroke at higher load. *Nature* **428,** 578-581.

Rief M, Gautel M, Oesterhelt F, Fernandez JM & Gaub HE. (1997). Reversible unfolding of individual titin immunoglobulin domains by AFM. *Science* **276,** 1109-1112.

Rivas-Pardo JA, Eckels EC, Popa I, Kosuri P, Linke WA & Fernandez JM. (2016). Work Done by Titin Protein Folding Assists Muscle Contraction. *Cell reports* **14,** 1339-1347.

Rome E, Offer G & Pepe FA. (1973). X-ray diffraction of muscle labelled with antibody to C-protein. *Nat New Biol* **244,** 152-154.

Sellers JR. (1999). *Myosins*. Oxford University Press, New York.

Sorimachi H, Kinbara K, Kimura S, Takahashi M, Ishiura S, Sasagawa N, Sorimachi N, Shimada H, Tagawa K, Maruyama K & et al. (1995). Muscle-specific calpain, p94, responsible for limb girdle muscular dystrophy type 2A, associates with connectin through IS2, a p94-specific sequence. *J Biol Chem* **270,** 31158-31162.

Stewart MA, Franks-Skiba K, Chen S & Cooke R. (2010). Myosin ATP turnover rate is a mechanism involved in thermogenesis in resting skeletal muscle fibers. *Proc Natl Acad Sci USA* **107,** 430-435.

Sun YB, Lou F & Edman KA. (1996). The relationship between the intracellular Ca2+ transient and the isometric twitch force in frog muscle fibres. *Exp Physiol* **81,** 711-724.

Tamura T, Wakayama J, Inoue K, Yagi N & Iwamoto H. (2009). Dynamics of thin-filament activation in rabbit skeletal muscle fibers examined by time-resolved x-ray diffraction. *Biophys J* **96,** 1045-1055.

Tonino P, Kiss B, Gohlke J, Smith JE, 3rd & Granzier H. (2019). Fine mapping titin's C-zone: Matching cardiac myosin-binding protein C stripes with titin's super-repeats. *J Mol Cell Cardiol* **133,** 47-56.

Trinick J. (1996). Titin as a scaffold and spring. Cytoskeleton. *Curr Biol* **6,** 258-260.

Trombitas K, Baatsen PH, Kellermayer MS & Pollack GH. (1991). Nature and origin of gap filaments in striated muscle. *J Cell Sci* **100 (Pt 4),** 809-814.

Trombitas K, Greaser M, Labeit S, Jin JP, Kellermayer M, Helmes M & Granzier H. (1998). Titin extensibility in situ: entropic elasticity of permanently folded and permanently unfolded molecular segments. *J Cell Biol* **140,** 853-859.

Tskhovrebova L, Trinick J, Sleep JA & Simmons RM. (1997). Elasticity and unfolding of single molecules of the giant muscle protein titin. *Nature* **387,** 308-312.

Wang K, McClure J & Tu A. (1979). Titin: major myofibrillar components of striated muscle. *Proc Natl Acad Sci USA* **76,** 3698-3702.

Woodhead JL, Zhao FQ, Craig R, Egelman EH, Alamo L & Padron R. (2005). Atomic model of a myosin filament in the relaxed state. *Nature* **436,** 1195-1199.

Zoghbi ME, Woodhead JL, Moss RL & Craig R. (2008). Three-dimensional structure of vertebrate cardiac muscle myosin filaments. *Proc Natl Acad Sci USA* **105,** 2386-2390.